A Preoptic Neurocircuit That Modulates Metabolic Flexibility

Julian M. Roessler[1,2,3,4], Matthew Alkire[1], Nathan Nigrin[1], Haorui Wang[1,5], Christopher M. Reid[1], Marissa D. Cortopassi[6], Millenia Waite[1], Brooke Linnehan[1], Eric C. Griffith[7], Mollie Madigan[8], Tenzin Kunchok[1], Alexander S. Banks[6], Fabian Schulte[1], Bukyung Kim[9], Bo-Yeon Kim[9], Jason K. Kim[9], Siniša Hrvatin[1,2,3,10,11*]

[1] Whitehead Institute for Biomedical Research; Cambridge, MA, USA

[2] Department of Biology, Massachusetts Institute of Technology; Cambridge, MA, USA

[3] Molecular and Cellular Neuroscience Program, Massachusetts Institute of Technology; Cambridge, MA, USA

[4]Laboratory for Mucosal Immunology, The Rockefeller University; New York, NY, USA

[5]Neuroscience Program, Columbia University; New York, NY, USA

[6] Division of Endocrinology, Diabetes, and Metabolism, Beth Israel Deaconess Medical Center and Harvard Medical School, Boston, MA, USA

[7]Department of Neurobiology, Harvard Medical School; Boston, MA, USA

[8] Department of Comparative Medicine, Massachusetts Institute of Technology; Cambridge, MA, USA

[9] Program in Molecular Medicine and Department of Medicine, Division of Endocrinology, Diabetes, and Metabolism, University of Massachusetts Chan Medical School; Worcester, MA, USA

[10]Department of Brain and Cognitive Sciences, Massachusetts Institute of Technology; Cambridge, MA, USA

[11] Howard Hughes Medical Institute, Massachusetts Institute of Technology, Cambridge, MA

*Correspondence: shrvatin@wi.mit.edu

Abstract

Precise, dynamic control of metabolic fuel usage in response to environmental challenges such as altered food availability or temperature change is essential for animal survival. In mammals, metabolic flexibility—the capacity to shift cellular metabolism between carbohydrate and fatty acid oxidation—is understood to be largely regulated by circulating hormones such as insulin and glucagon. However, the role of the central nervous system in coordinating fuel selection and tissue metabolic tuning remains underexplored. Here, we investigated the mechanisms that mediate metabolic reprogramming following the acute activation of torpor-associated glutamatergic Adcyap1+ torpor-regulating neurons in the anteroventral preoptic area ($avPOA^{Vglut2/PACAP}$). The activation of these neurons rapidly shifts whole-body fuel use from glucose to fatty acids, irrespective of fuel/food availability. This shift is associated with reduced glucose utilization stemming from the transient induction of selective insulin resistance in skeletal muscle. We find that this reduction in skeletal muscle glucose metabolism does not require direct muscle innervation but is rather mediated via adrenal hormones. In contrast to their activation, $avPOA^{Vglut2/PACAP}$ neuronal silencing results in improved glucose tolerance, demonstrating powerful bidirectional control of tissue-specific glucose metabolism, whole-body glucose levels, and fuel usage. Together, our findings uncover a novel POA-adrenal-skeletal muscle pathway that dynamically controls glucose utilization and metabolic flexibility.

63 **Introduction**

64 Dynamic control of metabolism is essential for homeostatic maintenance in response to
65 changing environments, including altered temperature, food availability, and stress. For example,
66 in the context of nutrient deficit or increased energetic demands, fuel usage shifts from mixed
67 fatty acid and carbohydrate oxidation to near complete reliance on fat metabolism to preserve
68 glucose for use by the brain and prevent hypoglycemia[1,2]. Metabolic inflexibility, the inability to
69 efficiently switch between these fuel sources, has been linked to obesity, diabetes, and metabolic
70 disease[3,4].

71 Baseline regulation of blood sugar and fuel usage is largely controlled by the circulating
72 pancreatic hormones insulin and glucagon, with insulin resistance representing a key aspect of
73 disease-associated metabolic inflexibility[3–5]. While these hormonal regulators of metabolic
74 flexibility and their peripheral effectors have been extensively studied, less is known concerning
75 the role of the central nervous system (CNS) in dynamic top-down metabolic control. The
76 ventromedial hypothalamus (VMH) is the primary nucleus in the brain known to control
77 systemic glucose usage. Activation of counterregulatory steroidogenic factor 1 (SF-1)- or
78 Cholecystokinin B receptor (CCKBR)-expressing neurons in the VMH drives increased levels of
79 systemic glucose and peripheral tissue insulin sensitivity[6,7]. In addition, brain-body signaling via
80 the hypothalamic-pituitary-adrenal (HPA) axis has long been known to play a crucial role in
81 stress-induced metabolic responses, influencing insulin sensitivity and energy balance[8,9]. Yet,
82 which neuronal populations and brain-body axes mediate dynamic metabolic reprogramming in
83 response to various environmental challenges remain to be fully characterized.

84 In response to prolonged periods of food deprivation, a wide range of mammalian
85 species, including laboratory mice (*Mus musculus*), have evolved the capacity to suspend or
86 override canonical fasting metabolism to enter protective hypometabolic states such as daily
87 torpor and hibernation[10]. Fasting-induced daily torpor in mice is characterized by a reduction of
88 metabolic rate by approximately 60%[2,10] and an accompanying reduction in body temperature
89 from 37°C to near ambient levels. It has long been appreciated that entry into and maintenance of
90 these states requires utilization of internal fat stores as a primary energy source, shifting
91 metabolism almost entirely towards fatty acid oxidation[2]. Recent work from our group and others
92 has shown that torpor entry is centrally controlled by the activity of glutamatergic neurons within
93 the anteroventral preoptic area of the hypothalamus (avPOA^{Vglut2} neurons). The activation of this

94 neuronal population results in a dramatic reduction in energy expenditure even in the absence of
95 caloric restriction, suggesting that these neurons are powerful modulators of systemic metabolic
96 flexibility [11,12,13]. Discrete activation of this circuit thus provides a means to dissect a central
97 pathway for controlling metabolic flexibility, without the confounding metabolic effects of
98 prolonged fasting.

99 Here, we leverage the power of targeted opto- and chemogenetic circuit manipulation to
100 probe the metabolic effects of avPOA^{Vglut2} neuronal activation in the mouse and trace
101 downstream consequences for peripheral organ-specific glucose regulation. We show that
102 avPOA^{Vglut2} neuronal activation drives a preferential reduction in whole-body glucose
103 metabolism and a shift to a fatty acid oxidative state stemming from acute tissue-specific skeletal
104 muscle and brown adipose tissue insulin resistance. Moreover, acute inhibition of this population
105 improves glucose tolerance, nominating avPOA^{Vglut2} neurons as powerful bidirectional regulators
106 of glucose homeostasis. The resulting reduction in skeletal muscle glucose uptake and systemic
107 glucose intolerance is not dependent on the decrease in core body temperature, nor direct muscle
108 innervation, but rather is hormonally driven by the adrenal glands. Furthermore, these effects are
109 recapitulated by the Adcyap1^{+} (PACAP-expressing) subpopulation of avPOA^{Vglut2} neurons.
110 Together, these findings identify avPOA^{Vglut2} neurons as a significant unappreciated CNS
111 glucoregulatory population intimately involved in the regulation of the overall metabolic state.
112 Targeted manipulation of this neuronal population and its downstream effectors may thus prove
113 relevant to the amelioration of disorders of metabolic inflexibility, such as obesity, diabetes, and
114 metabolic syndrome.
115

116 **Results**

117 **avPOA^{Vglut2} neurons control systemic metabolic fuel usage independent of changes in body**
118 **temperature**

119 Torpor is canonically understood as a strategy for energetic conservation during times of
120 nutrient deprivation[2]. While it is well-appreciated that fasting induces a shift from carbohydrate
121 oxidation (CHO) to fatty acid oxidation (FAO)[14], how torpor entry affects CHO versus FAO
122 utilization relative to surrounding periods of fasting at euthermic body temperatures remains less
123 well characterized. To monitor shifting fuel usage during fasting-induced torpor, 8-week-old
124 wild-type C57Bl/6J mice were implanted intraperitoneally with telemetric temperature probes,

125 fasted in metabolic cages for 24 hours, and monitored for changes in body temperature (T_b), gas
126 exchange, and respiratory exchange ratio (RER) — an established measure of CHO versus FAO
127 utilization (**Figure 1a)**. RER levels were found to decrease substantially during periods of torpor
128 relative to the fed state and surrounding periods of euthermic fasting (**Figure 1a, b)**, consistent
129 with an acute shift away from CHO and towards FAO during torpor.
130 We previously demonstrated that chemogenetic stimulation of avPOA neurons
131 phenocopies the decreased T_b and metabolic rate observed during natural torpor, thereby
132 providing a model to decouple avPOA neuronal activity from fasting-induced metabolic
133 changes[11]. To determine the metabolic consequences of avPOA neuronal activation, we
134 stereotactically introduced a neuronally targeted adeno-associated virus (AAV) expressing Gq-
135 DREADD[15] (AAV-hSyn-hM3D(Gq)-mCherry) into the avPOA of C57Bl/6J mice (**Figure 1c**).
136 The Gq-DREADD-activating ligand Clozapine-N-Oxide (CNO) was administered
137 intraperitoneally to these non-fasted animals, resulting in substantial decreases in both body
138 temperature and metabolic rate following CNO injection as compared to saline-injected control
139 animals (**Figures 1d-e, Supplementary Figures 1a,b**). These decreases were accompanied by
140 dramatic reductions in other metabolic parameters, including food intake, VCO_2, and VO_2
141 (**Supplementary Figures 1b-f**), as well as a marked shift in RER, from 0.86±0.01 to 0.66±0.02
142 (**Figure 1d**), consistent with a shift in metabolic fuel usage from mixed metabolism
143 (carbohydrate and fat) to primarily fat catabolism[3,16]. Moreover, utilizing the method of Frayn[16]
144 to quantify the relative contribution of CHO and FAO to overall energy expenditure, we
145 confirmed that upon avPOA stimulation animals transition from a mixed fuel state to nearly
146 exclusively using FAO for energy generation (**Figure 1g**). Together, these results demonstrate
147 that avPOA^{Vglut2} neuronal activation alone is sufficient to induce the alterations in fuel usage,
148 independent of caloric deprivation.
149 To determine whether the observed Gq-DREADD-driven RER effect was mediated by
150 decreased T_b, we increased the ambient temperature (T_a) from 24°C to 32°C, reasoning that
151 increased T_a would prevent the T_b decrease accompanying avPOA^{Vglut2} neuron activation.
152 Indeed, we observed that the average T_b of CNO-stimulated animals at this elevated ambient
153 temperature was 35.7±0.24°C as compared with 29.8±0.22°C when stimulated at T_a = 24°C
154 (**Figure 1h, Supplementary Figure 1e**). Strikingly, despite the absence of a large T_b drop,
155 stimulated animals exhibited a dramatic decrease in RER nearly identical to that observed at

156 24°C (**Figure 1h**), indicating that the observed metabolic shift is not a secondary consequence of
157 T_b reduction.
158
159 **avPOA^{Vglut2} neurons regulate blood glucose homeostasis and drive metabolic inflexibility**
160 To gain deeper insight into the metabolic consequences of avPOA neuronal stimulation,
161 we performed polar serum metabolomics analyses to identify changes in circulating metabolites
162 accompanying avPOA stimulation. Having previously identified glutamatergic avPOA
163 (avPOA^{Vglut2}) neurons as the primary drivers of torpid hypometabolism, we sought to target this
164 neuronal population more specifically. To this end, we transduced the avPOA of telemetric
165 probe-implanted *Vglut2-IRES-Cre* animals with AAV expressing either a Cre-dependent Gq-
166 DREADD or mCherry control. After collecting tail blood to establish a baseline for comparison,
167 animals were administered CNO, and blood samples were collected 15, 30, 60, and 120 minutes
168 post-injection, while continuously measuring T_b. We then performed plasma separation and polar
169 metabolome analysis on these samples, examining longitudinal changes in the abundance of
170 polar plasma metabolites in Gq-DREADD mice as compared with their mCherry counterparts
171 (**Figure 2a**). This analysis identified 4 significantly increased and 34 significantly decreased
172 polar plasma metabolites across all time points in avPOA^{Vglut2} neuron-stimulated animals
173 (**Figure 2b**). Observed changes involved significant decreases in key glycolytic and citric acid
174 cycle metabolites, including lactate, pyruvate, and 3-phosphoglycerate, accompanied by
175 increases in beta-hydroxybutyrate (**Figure 2b, Supplementary Figures 2a-d**). These changes
176 were monotonic across the duration of the experiment, suggesting continued suppression of
177 glucose metabolism (**Supplementary Figure 2a**), and were consistent with a state in which low
178 blood glucose levels lead to decreased glycolysis and a compensatory increase in FAO.
179 However, instead of a decrease in blood glucose levels, we observed an increase in serum
180 glucose (**Figure 2a**), suggesting that avPOA^{Vglut2} stimulation suppresses glucose metabolism
181 downstream of glucose availability. This suppression of glucose metabolism generates a
182 metabolically inflexible state, wherein animals rely nearly completely on fatty acid oxidation for
183 energy production.
184 Blood glucose levels are dynamically regulated by balancing glucose production through
185 hepatic gluconeogenesis and glycogenolysis with tissue glucose uptake via insulin-independent
186 and -responsive glucose transporters[17,18]. To test whether avPOA^{Vglut2} neuron stimulation resulted

187 in reduced glucose uptake, we subjected control (mCherry-injected) and experimental (Gq-
188 DREADD-injected) animals to a modified glucose tolerance test (GTT) following CNO
189 stimulation. Briefly, animals were fasted for 3 hours, administered CNO, and injected
190 intraperitoneally with a bolus of glucose (2 g/kg) 1 hour post-CNO stimulation (**Figure 2c**).
191 Strikingly, avPOA^{Vglut2} neuron-stimulated animals were significantly hyperglycemic at the end of
192 the test relative to their control counterparts (**Figures 2d-f**), indicating that avPOA^{Vglut2} neuron
193 stimulation induces pronounced systemic glucose intolerance. Consistent with our previously
194 observed effects on RER (**Figure 1f**), this glucose intolerance effect was not dependent on
195 decreased body temperature, as raising the ambient temperature (T_a = 32°C) failed to restore
196 glucose tolerance in these torpid mice (**Figure 2e-f**).
197 This finding led us to hypothesize that the effect of these neurons could be bidirectional,
198 and that inhibition of these neurons may improve glucose tolerance. To test this idea, we
199 transduced *Vglut2-IRES-Cre* animals with a Cre-dependent inhibitory Gi-DREADD (AAV-
200 hSyn-DIO-hM4D(Gi)-mCherry). To confirm effective targeting, we fasted Gi-DREADD-
201 transduced animals and observed that, as expected, upon CNO administration, Gi-DREADD-
202 mediated silencing of avPOA^{Vglut2} neurons was sufficient to prevent torpor entry
203 (**Supplementary Figures 2e, f**). To investigate the effects of avPOA^{Vglut2} neuronal silencing on
204 glucose tolerance, we first performed a baseline GTT in which mice were pretreated with PBS
205 and after one week of recovery, the same animals were pretreated with CNO and administered a
206 second GTT. Remarkably, acute inhibition of avPOA^{Vglut2} neurons resulted in increased glucose
207 tolerance, as peak glucose levels were significantly lower following CNO injection as compared
208 to PBS (PBS $Glucose_{Max}$ = 361.7 ± 11.4 mg/dL, CNO $Glucose_{Max}$ = 296.9 ± 12.4 mg/dL), and
209 remained consistently lower throughout the duration of the assay (**Figures 2h, i**). These findings
210 suggest that avPOA^{Vglut2} neuronal activity can bidirectionally control systemic glucose tolerance.
211 To examine the kinetics of this induced glucose intolerance, we transduced the avPOA of
212 *Vglut2-IRES-Cre* mice with AAV expressing either a Cre-dependent Channelrhodhopsin-2
213 (ChR2) (AAV-DIO-ChR2(H134R)-EYFP) or an EYFP (AAV-DIO-EYFP) control, and
214 subsequently implanted an optic fiber above the avPOA (**Figure 2j**). After surgical recovery, we
215 monitored plasma glucose and T_b over the course of 40 minutes of optogenetic blue light
216 stimulation (16 Hz, 8.5 mW, 1s on 1s off) as well as for an additional 40 minutes post-
217 stimulation. Optogenetic stimulation of avPOA^{Vglut2} neurons resulted in the anticipated decrease

218 in body temperature, as well as a rapid, monotonic increase in blood glucose not observed in the
219 EYFP controls (**Figures 2k-l, Supplementary Figure 2f**). Notably, upon light cessation, blood
220 glucose levels and T_b rapidly returned to normal, demonstrating that glucose intolerance is a
221 rapid, transient, and reversible effect of avPOA^{Vglut2} neuronal stimulation. Together, our findings
222 identify avPOA^{Vglut2} neurons as a significant glucoregulatory population that contributes to rapid,
223 reversible modulation of glucose homeostasis, drives a torpor-associated metabolic shift from
224 glucose metabolism towards fatty acid catabolism upon stimulation, and bidirectionally regulates
225 glucose tolerance upon activation or inhibition.
226
227 **avPOA^{Vglut2} neuronal activation drives insulin resistance and reduces glucose uptake**
228 Dysregulation of glucose homeostasis is often secondary to either reduced insulin
229 secretion or reduced insulin action on peripheral tissues in response to glucose challenge[17]. To
230 test whether the observed avPOA^{Vglut2} neuron-induced dysregulation of glucose clearance was a
231 consequence of reduced insulin secretion, we assessed circulating insulin levels in the context of
232 our GTT experimental paradigm. Remarkably, we observed no significant differences in insulin
233 levels in CNO-stimulated Gq-DREADD-expressing animals relative to mCherry controls
234 (**Supplementary Figure 3a**), suggesting that glucose-stimulated insulin secretion (GSIS) is
235 unaffected by avPOA^{Vglut2} neuronal stimulation. These findings were further confirmed by
236 monitoring GSIS in both Gq-DREADD-expressing and control mice in the context of a
237 hyperglycemic clamp[19] (**Supplementary Figure 3b**). Indeed, even the elevated insulin levels
238 observed in Gq-DREADD-expressing mice could not normalize plasma glucose in these animals
239 following CNO-stimulation, suggesting that avPOA^{Vglut2} neuron stimulation induces systemic
240 insulin insensitivity.
241 To further investigate this avPOA^{Vglut2} neuronal stimulation-induced insulin insensitivity,
242 we performed hyperinsulinemic-euglycemic clamp studies in Gq-DREADD-expressing *Vglut2-*
243 *IRES-Cre* mice and corresponding mCherry control animals following CNO stimulation (**Figure**
244 **3a**). Briefly, in both Gq-DREADD- and mCherry-expressing animals, we induced
245 hyperinsulinemia via constant insulin infusion while concomitant glucose infusion at a variable
246 rate was used to maintain euglycemia[20]. Importantly, all animals were partially restrained during
247 these studies for the purposes of blood sampling. This afforded us an ability to control for the

248 reduced locomotor activity of avPOA^{Vglut2} neuron-stimulated mice as compared to their
249 unstimulated control counterparts (see **Methods**).
250 Although euglycemia was achieved in both the Gq-DREADD-expressing and control
251 cohorts, the glucose-infusion rate (GIR) to maintain euglycemia during the insulin clamp
252 experiments in Gq-DREADD-expressing animals was significantly lower than that of controls,
253 indicating reduced insulin sensitivity (**Figures 3b, c)**. Moreover, while hepatic glucose
254 production during the insulin clamp was unaffected by avPOA^{Vglut2} neuronal stimulation, both
255 whole-body glucose turnover and glycolysis were dramatically reduced (**Supplementary**
256 **Figures 3f-i**), consistent with our observed metabolomics results in which circulating glycolytic
257 and TCA cycle metabolites were reduced by avPOA^{Vglut2} neuron stimulation. Taken together, our
258 findings show that avPOA^{Vglut2} neuronal activation induces systemic insulin resistance in mice,
259 thereby contributing to reduced glucose metabolism in these animals.
260
261 **avPOA^{Vglut2} neurons control organ-specific changes in glucose uptake**
262 To characterize the individual organs responsible for systemic insulin resistance, a bolus
263 of the non-metabolizable glucose analogue, ^{14}C-2-deoxy-glucose (^{14}C-2DG), was intraperitonelly
264 injected during the hyperinsulinemic-euglycemic clamp experiments. At the conclusion of the
265 experiments, animals were sacrificed, and liver, brain, white adipose tissue (WAT), brown
266 adipose tissue (BAT), heart, and gastrocnemius muscle were collected for biochemical analysis
267 of their ^{14}C-2DG-6-phosphate content. Scintillation counting revealed no significant changes in
268 the insulin-stimulated glucose uptake rate of heart, WAT, and brain. However, there was a
269 marked reduction in glucose uptake in both gastrocnemius muscle and BAT from avPOA^{Vglut2}
270 neuron-stimulated animals (**Figures 3d, e**), indicating organ-specific changes in insulin action
271 and glucose metabolism.
272 We calculated total glucose uptake in the presence or absence of avPOA^{Vglut2} neuronal
273 stimulation for each of the six tested tissues based on our measured rates of glucose uptake and
274 tissue weights. Consistent with prior findings that skeletal muscle accounts for ~80% of post-
275 prandial glucose utilization, and up to 75% of glucose disposal upon infusion[21], this analysis
276 revealed that diminished skeletal muscle glucose uptake accounts for a large fraction of the total
277 glucose utilization deficit observed in avPOA^{Vglut2} neuron-stimulated animals (**Figure 3f**),
278 suggesting that effects on skeletal muscle are the major contributor to the avPOA^{Vglut2} neuron-

279 driven impairment of insulin sensitivity. Importantly, we confirmed that this decrease in skeletal
280 muscle glucose uptake was not dependent on body temperature changes (**Figures 4a, b**). In
281 addition, comparative phospho-proteomic analysis of gastrocnemius samples from avPOA^{Vglut2}
282 neuron-stimulated and control animals provided evidence of avPOA^{Vglut2} neuron-driven
283 suppression of skeletal muscle insulin signaling (**Supplementary Figure 4**). Given these
284 findings, we focused our subsequent investigation of the peripheral effects of avPOA^{Vglut2} neuron
285 activation on skeletal muscle.
286
287 **avPOA^{Vglut2} neuronal control of muscle glucose uptake occurs independent of muscle**
288 **innervation**
289 We next sought to determine the manner by which avPOA^{Vglut2} neurons convey
290 glucoregulatory signals to the periphery (**Figure 4a**). In this regard, skeletal muscle is innervated
291 by both sympathetic nervous system (SNS) and motor nervous system (MNS) fibers[22], and
292 sympathetic activation has been previously shown to enhance skeletal muscle glucose uptake via
293 the β-adrenergic signaling, primarily through β2-adrenergic receptors[23]. We therefore employed
294 a genetic approach to test the requirement for β-adrenergic sympathetic signaling in avPOA^{Vglut2}
295 neuron-driven changes in glucose tolerance, utilizing mice lacking β_1- and β_2-adrenergic
296 receptors ($\beta_{1/2}$-KO). For these studies, a *CaMKIIa* promoter-driven AAV (AAV-CaMKIIa-
297 hM3D(Gq)-mCherry) was used to achieve selective Gq-DREADD expression in excitatory
298 avPOA neurons of $\beta_{1/2}$-KO and wild-type control mice. To ensure that our results with this
299 *CaMKIIa* approach were consistent with our *Vglut2-IRES-Cre* experiments, we compared
300 expression patterns and GTT results of *CaMKIIα*-Gq-injected animals with those of Cre-
301 dependent *Vglut2-IRES-Cre* animals and found no significant differences in expression nor
302 glucose intolerance between cohorts (**Supplementary Figures 5a, b**). Following CNO
303 stimulation, we performed a GTT assay on these animals, which revealed no significant
304 differences in CNO-stimulated glucose intolerance between Gq-DREADD-expressing $\beta_{1/2}$-KO
305 and wild-type animals (**Figure 4c**), suggesting that $\beta_{1/2}$ adrenergic receptors were not required
306 for avPOA^{Vglut2} glucoregulatory signaling. As an orthogonal approach, we also performed
307 chemical sympathetic inhibition in Gq-DREADD-expressing *Vglut2-IRES-Cre* mice via the
308 sympatholytic drug guanethidine, which enters noradrenergic terminals and displaces
309 norepinephrine from synaptic vesicles to suppress norepinephrine release[24]. As expected, given

310 its vasodilatory properties, guanethidine treatment alone increased baseline glucose tolerance
311 compared with PBS. However, despite SNS inhibition by guanethidine, avPOA^{Vglut2} activation
312 still induced glucose intolerance (**Figure 4d**). Taken together, these genetic and pharmacological
313 studies strongly suggest that SNS activity is dispensable for avPOA^{Vglut2} neuron-driven glucose
314 intolerance.

315 Motor innervation and movement also serve as well-appreciated regulators of glucose
316 metabolism[18]. To test the role of motor innervation on glucose uptake during avPOA^{Vglut2}
317 neuronal stimulation, we performed unilateral sciatic nerve denervations in mCherry control and
318 Gq-DREADD-transduced *Vglut2-IRES-Cre* mice[25]. This approach allowed us to compare, within
319 the same animal, the effects of avPOA^{Vglut2} neuron stimulation on muscle glucose uptake in the
320 innervated and the denervated limb (**Figure 4e**). Unilaterally denervated animals were injected
321 with CNO 1 hour prior to administration of the nonmetabolizable radioactive glucose analog ^{3}H-
322 2-Deoxyglucose. The animals were then monitored for changes in blood glucose and radioactive
323 substrate availability for 30 minutes, sacrificed, and their ipsi- and contra-lateral gastrocnemius
324 muscles processed for scintillation counting of ^{3}H-2-DG-6-Phosphate. As expected, denervated
325 gastrocnemius muscle exhibited reduced glucose uptake relative to the contralateral innervated
326 muscle under basal conditions (**Figure 4f**). Importantly, both innervated and denervated muscles
327 exhibited similarly pronounced reductions in glucose uptake following CNO-mediated
328 avPOA^{Vglut2} neuronal stimulation, with no significant differences in the ratio of CNO-stimulated
329 to baseline glucose uptake in the innervated and denervated muscle (**Figure 4f**). Taken together,
330 these results demonstrate that sympathetic innervation and direct motor innervation are
331 dispensable for avPOA^{Vglut2} neuron-driven changes in muscle glucose uptake.
332

333 **Adrenal hormones contribute to the avPOA^{Vglut2}-induced reduction of muscle glucose**
334 **uptake**

335 Given the apparent dispensability of direct muscle innervation for avPOA^{Vglut2} neuron-to-
336 skeletal muscle signaling, we examined the potential involvement of known circulating
337 glucoregulatory hormones, assessing insulin, glucagon, leptin, and corticosterone plasma levels
338 in Gq-DREADD- and mCherry-transduced animals by ELISA following treatment with CNO
339 (**Figure 4g**). While no significant differences in insulin, glucagon, or leptin levels were
340 associated with avPOA^{Vglut2} neuronal stimulation (**Figure 4g**), we observed a ~2.5-fold increase

341 in plasma corticosterone levels in Gq-DREADD-expressing animals up to 2 hours post-CNO
342 stimulation, as compared with baseline (**Figure 4g**). The increase in corticosterone tracked well
343 with the observed increase in glucose levels (**Figure 4h**), suggesting a potential role for
344 circulating corticosterone levels in avPOA^{Vglut2} neuron-induced glucose uptake changes.
345 Corticosterone functions as a glucoregulatory stress hormone and is secreted from the
346 adrenal cortex upon activation of the hypothalamic-pituitary-adrenal axis (HPA)[8,9]. To test
347 whether avPOA^{Vglut2} neuron-driven glucose intolerance requires corticosterone, we obtained
348 bilateral adrenalectomized (Admex) or sham adrenalectomized (Sham) wild-type C57/B6N mice
349 and validated the efficacy of the adrenalectomy procedure by measuring plasma corticosterone
350 levels (**Figure 5a**). Animals exhibiting normal levels of corticosterone were excluded from
351 further analysis. Admex and sham surgery control mice were stereotactically administered a
352 *CaMKIIa* promoter-driven Gq-DREADD AAV (AAV-CaMKIIa-hM3D(Gq)-mCherry) to
353 achieve selective Gq-DREADD expression in predominantly excitatory avPOA neurons. We
354 first confirmed that CaMKIIa-driven Gq-DREADD stimulation in sham control animals
355 phenocopied the glucose intolerance observed upon Cre-dependent avPOA^{Vglut2} stimulation in
356 *Vglut2-IRES-Cre* mice (**Supplementary Figure 5a**). Further investigation revealed that CNO-
357 mediated avPOA^{Vglut2} neuronal stimulation induced similar decreases in body temperature in
358 both Admex and sham control animals (**Figure 5b**). While GTT assays revealed no differences
359 in baseline glucose tolerance between Admex and sham control animals in the absence of CNO
360 stimulation (**Supplementary Figure 5b**), the characteristic glucose intolerance observed in sham
361 animals following CNO stimulation was completely absent in the adrenalectomized animals
362 (**Figure 5c**), strongly suggesting that adrenal-derived hormones are required for avPOA^{Vglut2}-
363 driven glucose intolerance.
364 To directly test the contribution of corticosterone to avPOA^{Vglut2} neuron-induced glucose
365 intolerance, we utilized metyrapone, an inhibitor of corticosterone synthesis (**Figure 5d**)[26].
366 Baseline blood samples from unstimulated Gq-DREADD-expressing *Vglut2-IRES-Cre* mice
367 confirmed that metyrapone administration significantly decreased serum corticosterone levels
368 relative to saline-treated controls (**Figure 5e**). Subsequent GTT assays showed that metyrapone
369 treatment significantly attenuated CNO-induced glucose intolerance in Gq-DREADD-expressing
370 animals (**Figures 5f, g**). Although incomplete, this reversal of glucose intolerance in

371 metyrapone-treated animals identifies adrenal-derived corticosterone as a major regulator of
372 glucose homeostasis downstream of avPOA^{Vglut2} neuronal activation.
373
374 **avPOA^{PACAP} neuronal activity is sufficient to drive avPOA glucoregulatory effects**
375 Having outlined this POA-to-muscle glucoregulatory signaling axis, we sought to better
376 define the neuronal population within the POA that underlies these glucoregulatory effects. To
377 begin to address this question, we performed axon terminal and monosynaptic anterograde
378 mapping of downstream avPOA^{Vglut2} target regions (**Figure 6a, Supplementary Figures 6a,**
379 **b**)[27]. Both mapping approaches revealed the dorsomedial hypothalamus (DMH) and Raphe
380 Pallidus (RPa) as densely innervated by avPOA^{Vglut2} neurons. These regions have been heavily
381 implicated in control of metabolic rate and thermogenesis[28,29]. To test their role in avPOA^{Vglut2}
382 neuron-driven regulation of glucose homeostasis, we optogenetically stimulated axonal terminals
383 of avPOA^{Vglut2} neurons transduced with Cre-dependent ChR2 in either the DMH or RPa and
384 analyzed the effects on blood glucose tolerance. Despite dense axonal labeling in the RPa,
385 stimulation of avPOA^{Vglut2} neuron terminals in this region failed to induce glucose intolerance
386 (**Figure 6c**). By contrast, stimulation of DMH-projecting neurons fully phenocopied the glucose
387 intolerance induced by avPOA soma stimulation (**Figure 6c**), indicating that excitatory
388 avPOA->DMH projections are sufficient to drive acute glucose intolerance.
389 In addition to the anatomical heterogeneity of its projections, the avPOA glutamatergic
390 neuronal population is comprised of molecularly diverse neuronal subpopulations that could
391 mediate distinct effects on physiology[30]. In this regard, we initially focused on Adcyap1
392 (PACAP)- and Leptin Receptor (LepR)-expressing neurons given the established involvement of
393 these two largely excitatory POA neuronal subpopulations in metabolic and thermoregulatory
394 programs[13,31]. Integrated analysis of our prior single-nucleus transcriptomic data[11], showed that
395 *Adcyap1*+ neurons largely constitute a subset of POA glutamatergic neurons present throughout
396 the anatomical length of the POA, whereas LepR+ neurons form a distinct but molecularly
397 overlapping population with *Adcyap1* neurons located primarily in the anterior portion of the
398 POA (**Figures 6d, e**). To determine whether chemogenetic stimulation of one or both of these
399 subpopulations was sufficient to give rise to avPOA^{Vglut2}-associated glucoregulatory effects, we
400 stereotactically introduced our Cre-dependent AAV expressing Gq-DREADD into the avPOA of
401 *Adcyap1-2A-Cre* (avPOA^{PACAP}) or *Lepr-IRES-Cre* (avPOA^{LepR}) animals. Subsequent

402 chemogenetic stimulation of both avPOA^{PACAP} and avPOA^{LepR} neurons fully phenocopied the
403 glucose intolerance observed upon avPOA^{Vglut2} neuronal stimulation (**Figures 6f-h**),
404 demonstrating that either avPOA^{PACAP} or avPOA^{LepR} neuronal stimulation is sufficient to give
405 rise to the glucoregulatory effects of the broader avPOA^{Vglut2} population.
406 Given these results implicating PACAP^{+} avPOA neurons in the regulation of blood
407 glucose homeostasis, we sought to demonstrate their importance in regulating organismal
408 metabolic flexibility. To this end, we repeated our prior polar metabolomics approach done in
409 *Vglut2-IRES-Cre* animals with *PACAP-2A-Cre* mice that were stereotactically transduced with
410 Cre-dependent mCherry or Gq-DREADD AAVs, and upon recovery subjecting these animals to
411 blood collection and metabolic profiling following CNO stimulation. Consistent with the results
412 observed under avPOA^{Vglut2} neuronal stimulation, we observed significant decreases in the
413 abundance of major glycolytic and citric acid cycle metabolites when comparing avPOA^{PACAP}
414 Gq-DREADD-stimulated and control avPOA^{mCherry} animals 120 minutes after CNO
415 administration, including pyruvate, citrate, succinate, lactate, and malate (**Figure 6i**). Moreover,
416 consistent with increased reliance on fatty acid oxidation for fuel, we observed significant
417 increases in β-hydroxybutyrate in Gq-DREADD-stimulated avPOA^{PACAP} animals. There was
418 also a modest but non-significant increase in glucose abundance in these same animals 120
419 minutes post-stimulation. Analysis of earlier time points revealed a significant increase in blood
420 glucose in Gq-DREADD- vs. mCherry-expressing avPOA^{PACAP} animals at the 60-minute time
421 point (**Supplementary Figures 6d, e**), consistent both with our results in *Vglut2-IRES-Cre*
422 animals and a model in which avPOA^{PACAP} neurons directly regulate glucose tolerance. Finally,
423 we observed significant increases in the abundance of palmitate and α-lipoic acid at this time
424 point, indicating an increased mobilization of fat reserves to provide fuel via FAO during
425 avPOA^{PACAP} neuron stimulation. These results, coupled with our previous metabolomics
426 experiments in *Vglut2-IRES-Cre* animals, confirm that avPOA^{Vglut2} neurons are powerful
427 regulators of metabolic flexibility, and that avPOA^{PACAP} neurons are a Vglut2^{+} subtype sufficient
428 to drive this metabolic switch from carbohydrate to fatty acid catabolism.
429
430 **Discussion**
431 The ability to dynamically switch between metabolic fuel sources in the face of changing
432 nutrient availability and energetic demands is an essential feature of metabolic regulation.

433 Classically, this metabolic flexibility was understood to be driven mainly by circulating
434 hormonal factors, such as insulin and glucagon, with less known regarding the role of the central
435 nervous system in the control of whole-body and organ-specific fuel usage. Here, we focus on a
436 population of neurons associated with torpor and heat-defense to probe the mechanisms by
437 which CNS signals drive rapid systemic metabolic reprogramming in response to environmental
438 challenge. Surprisingly, we find that avPOA^{Vglut2} neuronal activation not only regulates whole-
439 body metabolic flexibility, but also controls fuel uptake and catabolism in an organ-specific
440 manner. Through a variety of interventions, we show that these effects are mediated via the
441 induction of acute insulin insensitivity in skeletal muscle and brown adipose tissue. In skeletal
442 muscle, this effect does not require sympathetic nervous system or motor neuron input. Rather,
443 the glucoregulatory effects of avPOA^{Vglut2} neurons appear to be mediated by adrenal hormones,
444 including corticosterone. Strikingly, acute silencing of this avPOA^{Vglut2} population was also
445 found to improve glucose tolerance, demonstrating that these neurons exert bidirectional control
446 over systemic glucose homeostasis and metabolic flexibility. While circuits regulating glucose
447 homeostasis and the counter-regulatory response to fasting have been described in other brain
448 regions[6,7,32], it is notable that the effects of avPOA^{Vglut2} activation and silencing on plasma
449 glucose levels exceed those of other known glucoregulatory circuits, suggesting that avPOA^{Vglut2}
450 neurons may be among the most potent central regulators of glucose homeostasis identified to
451 date.
452 Torpor is the primary physiological paradigm in which avPOA^{Vglut2} neuron function has
453 been described, and represents a dramatic challenge to normal thermal and metabolic
454 homeostasis[11,12]. In addition to their glucoregulatory capacities, activation of these neurons
455 results in profound hypothermia and hypometabolism, which are understood to be protective
456 adaptations for organismal survival[2]. One core aspect of this hypometabolism has been
457 hypothesized to be the preservation of glucose for the brain via reduction in peripheral organ
458 glucose uptake. However, until recently, it was unclear whether these neurons played an active
459 role in shaping specific, regulated aspects of this hypometabolic state, or if torpid metabolism
460 was secondary to decreases in T_b. Notably, a recent study examining a molecularly distinct
461 subpopulation of avPOA^{Vglut2} neurons expressing the neuropeptide QRFP (avPOA^{QRFP} neurons)
462 found that activation of this subpopulation results in both torpor-induction and impaired
463 glucoregulation, similar to avPOA^{Vglut2} neurons described in this work[33]. However, unlike our

464 findings, the researchers reported that avPOA^{QRFP} glucoregulation is secondary to body
465 temperature decreases. Our work shows that this is not a general principle of avPOA^{Vglut2}
466 neuron-mediated glucoregulation. In this regard, while avPOA^{Vglut2} stimulation in
467 adrenalectomized animals results in a nearly identical T_b decrease as that observed in animals
468 with intact adrenal glands, we do not observe an induction of glucose intolerance in these
469 adrenalectomized animals. Moreover, metabolic cage, GTT, and tissue-specific glucose uptake
470 experiments performed at elevated T_a, where animal T_b minimally decreases during avPOA^{Vglut2}
471 neuronal stimulation, all failed to ameliorate the observed glucose intolerance and uptake
472 defects. These divergent results suggest that there may be distinct subpopulations of avPOA^{Vglut2}
473 neurons which have temperature-dependent and -independent effects on glucose homeostasis.
474 Our data suggest a model in which activation of avPOA$^{Vglut2/PACAP}$ neurons contributes to
475 the reduction of glucose uptake in two of the primary consumers of glucose – skeletal muscle
476 and brown adipose tissue – thereby conserving glucose for uptake by the brain. Reduction of
477 glucose uptake in these tissues, coupled with peripheral reliance on fat stores and ketone bodies,
478 may allow for the stabilization of glucose levels such that the animal has sufficient available
479 energy stores to forage for food upon exit from torpor. While our results agree with studies of
480 overnight fasting that demonstrate relative insulin resistance and glucose intolerance compared
481 to mice with ad-libitum access to food[34], several glucoregulatory modalities (including changes
482 to insulin and glucagon levels) regulate glucose levels during fasting. Thus, further studies will
483 be needed to better understand the physiological benefit of avPOA$^{Vglut2/PACAP}$-mediated
484 glucoregulation during torpor. Moreover, avPOA^{PACAP} neurons have been implicated in
485 glucoregulation during warm challenge[35], and are involved in diverse behaviors, including sleep,
486 thirst, and cold-defense[31-37]. Future studies should examine the extent to which these neurons
487 regulate metabolic flexibility across these diverse physiological states.
488 An interesting aspect unaddressed by this study is what sensory modalities serve to
489 engage the activity of these neurons. Do these neurons respond directly to changes in circulating
490 hormone levels or metabolite abundance to trigger glucoregulatory metabolic shifts? Are there
491 ascending interoceptive neurocircuits that signal whole-body or tissue-specific nutrient
492 requirements to avPOA$^{Vglut2/PACAP}$ neurons? Future studies will be required to determine the
493 extent to which the glucoregulatory effects of these neurons impact mouse physiology during

494 these and other phenomenologically diverse states, and which sensory modalities trigger their
495 activation.
496 Intriguingly, this hypothalamic circuitry is largely conserved in non-torpid mammals,
497 including humans. Indeed, activation of avPOA^{Vglut2} neurons has been shown to induce torpor-
498 like hypometabolic state in the rat, a non-torpid animal[12]. Moreover, single-cell profiling of
499 avPOA subpopulations in non-human primates, such as marmosets, has revealed the presence of
500 avPOA$^{Vglut2/PACAP}$ neurons in the preoptic area of these animals (**Supplementary Figure 7**)[38,39].
501 While the function of these neurons in marmoset thermo- and gluco-regulation remains
502 unexplored, the anatomical and molecular conservation of these neurons in the preoptic area
503 suggests that they could have similar roles in regulating marmoset metabolic flexibility and
504 metabolic homeostasis. In humans, metabolic inflexibility is primarily understood within
505 pathological states such as diabetes, obesity, and metabolic syndromes, in which desensitization
506 mechanisms render peripheral tissues unable to respond to physiological levels of
507 glucoregulatory hormones such as insulin and leptin[21,36]. However, our findings raise the
508 possibility that such metabolic states can also be initiated or augmented by top-down
509 hypothalamic signaling. Future investigation will determine whether systematic changes in the
510 activity of these circuits over time predispose individuals to these disorders and facilitate the
511 development of metabolic pathologies.
512
513 **Methods and Materials**
514 **Mice**
515 Animal experiments were approved by the National Institutes of Health, Massachusetts Institute
516 of Technology's Committee on Animal Care (CAC), and Beth Israel Deaconess Medical
517 Center's IACUC following ethical guidelines described in the US National Institutes of Health
518 Guide for the Care and Use of Laboratory Animals. For initial metabolic cage experiments, we
519 used adult (8-12-week-old) C57BL/6J mice (The Jackson Laboratory, Stock 000664). For
520 natural, chemogenetic, and optogenetic torpor experiments, we used 8-12-week-old *Vglut2-*
521 *IRES-Cre* (The Jackson Laboratory, Stock 028863), *Adcyap1-2A-Cre* (The Jackson Laboratory,
522 Stock 030155), and *Lepr-IRES-Cre* (The Jackson Laboratory, Strain 008320) mice. For
523 adrenergic necessity experiments, we utilized 8-12-week-old β1/β2-KO animals (The Jackson
524 Laboratory, Stock 003810). Finally, for adrenalectomy experiments, we utilized C57BL/6J mice

525 from Jackson Labs, as well as C57BL/6N animals from Charles River (Charles River
526 Laboratories, Strain 027). Adrenalectomies were performed at The Jackson Laboratory or
527 Charles River Labs, respectively, and animals were provided 1% saline water to maintain
528 osmotic homeostasis as per the recommendation of the supplier. All mice were housed at 22°C
529 under a standard 12 h light/dark cycle until they were subjected to surgery, at which point they
530 were housed under a reversed 12 h light/dark cycle. Power analysis was used to predetermine
531 sample size, where appropriate (e.g radioactive glucose uptake as well as hyperinsulinemic-
532 euglycemic clamp experiments). Mice were randomly assigned to experimental groups before
533 surgery. Where possible, investigators were blinded during analysis.
534
535 **Telemetric monitoring of core body temperature and gross motor activity**
536 Mice were implanted abdominally with telemetric temperature and activity probes (Unified
537 Information Devices, UCT-2112). After at least four days of recovery, animals were singly
538 housed and recorded in standard cages placed onto a radiofrequency receiver platform (Unified
539 Information Devices, UID Mouse Matrix). Core body temperature and gross motor activity were
540 logged every 300 ms based on animal movement and averaged over either 1- or 5-minute
541 windows, as appropriate. Temperature data were collated and exported from the MouseMatrix
542 Software (Unified Information Devices, MouseMatrix 1.6.2) for downstream processing.
543 Analysis of temperature data was performed in R (R Core Team) using a custom-written R
544 Script.
545
546 **Metabolic cage experiments**
547 Metabolic cage data was collected on individually housed mice placed in a Promethion
548 indirect calorimeter (Sable Systems) with a temperature-controlled cabinet (Pol-Eco) and
549 provided with ad libitum food (Labdiet 5008) and water purified by reverse osmosis. Starr
550 Scientific telemetry receiver bases were placed beneath the Promethion Cages to match the
551 implanted probes. Mice were maintained under 12 h light/dark photoperiods (0600–1800) at an
552 ambient temperature of 23 ± 0.2°C. Position and physical activity were collected every second.
553 Rates of oxygen consumption (VO_2) and carbon dioxide production (VCO_2) were measured
554 every 2 min. Energy expenditure was calculated with the Weir equation[40].
555

556 **Fasting-inducted torpor**

557 Telemetric temperature probe-implanted adult (8-18-week-old) mice were singly housed before
558 the induction of torpor. Each mouse was moved to a new individual cage containing water and
559 nesting material but devoid of bedding and food at the beginning of the dark cycle (ZT 11.5).
560 Initial bouts of torpor were observed after approximately 8-12 h of fasting. Mice were returned to
561 their standard cages containing food 24 h after the start of the fast. The ambient temperature of
562 the facility was maintained at ~22°C.

563

564 **Stereotactic viral injection and fiber implantation**

565 For injections, mice were anaesthetized with 3% isoflurane and placed in a stereotaxic head
566 frame (Kopf Instrument, model 1900). Animals were kept constantly sedated using 1-1.5%
567 isoflurane, and either Buprenorphine SR (1.0 mg/kg) or Ethiqa SR (3.25 mg/kg) were
568 administered for analgesia. The skull was leveled in the AP and ML directions, and bore holes
569 were drilled using a stereotaxic drill (David Kopf Instruments). For chemogenetic experiments,
570 unless otherwise specified, craniotomies and viral administration were bilateral. For
571 optogenetics, craniotomies and viral administration were unilateral. An air-based injection
572 system built with Digital Manometer (Grainger, 9LHH8) was used to infuse the virus through
573 pulled glass capillaries. Virus was administered at the following coordinates - POA: AP +0.4
574 mm, ML ±0.5 mm, DV −5.02 mm, PVH: AP -1.0 mm, ML ±0.1 mm, DV −4.5mm, DMH: AP -
575 1.8 mm, ML ±0.5 mm, DV −5.02 mm, PAG: AP -3.25 mm, ML ±0..25 mm, DV −1.8 mm, RPa:
576 AP -5.5 mm, ML ±0.0 mm, DV −5.75 mm. Virus was infused at approximately 100 nL min^{-1},
577 and the needle was kept at the injection site for 10 min before withdrawal. Unless otherwise
578 specified, 100 nL of virus was administered per site (unilateral: 100 nL total, bilateral 200 nL
579 total). Following needle removal, the incision was closed using 4-0 monocryl adsorbable suture
580 (Ethicon) with alternating box knots in an interrupted pattern.

581 For optic fiber implantation for optogenetics, 400 μm, 0.37 NA borosilicate mono fiber
582 optic cannulae (Doric, MFC_400/430-0.37_###_MF1.25_FLT, where ### corresponds to fiber
583 length) were implanted approximately 500 μm above the injection site. Fibers were initially
584 fixed to the head using superglue (Gorilla Super Glue Gel), followed by Metabond (CB
585 Metabond S380) to ensure the stability of the implant. For optogenetics experiments, 100 nL of a
586 1:1 mixture of AAV8-hSyn-DIO-hM3D(Gq)–mCherry, or AAV8-hSyn-DIO-hM3D(Gq)–

587 mCherry and AAV8-EF1a-ChR2(H134R)-EYFP, respectively, were injected unilaterally into the
588 POA. Chemogenetic stimulation of POA neurons followed by monitoring of core temperature
589 decreases was used to validate injection accuracy. Animals not demonstrating temperature
590 reductions upon administration of CNO were removed from the analysis.
591
592 **Viral constructs**
593 AAV8-hSyn-DIO-hM3D(Gq)-mCherry (Addgene, 44361-AAV8), AAV-hSyn-fDIO-
594 hM3D(Gq)-mCherry-WPREpA (Addgene, 154868-AAV8), pAAV-EF1a-double floxed (DIO)-
595 hChR2(H134R)-EYFP-WPRE-HGHpA (Addgene, 20298-AAV1), pAAV-hSyn-DIO-
596 hM4D(Gi)-mCherry (Addgene, 44362-AAV8), AAV-CaMKIIa-hM3D(Gq)-mCherry (Addgene,
597 50476-AAV8), AAV-hSyn-hM3D(Gq)-mCherry (Addgene, 50474-AAV8), AAV-hSyn-DIO-
598 mCherry (Addgene, 50459-AAV8), and pAAV-hSyn-DIO-EGFP (Addgene, 50457-AAV8) were
599 obtained from Addgene. AAV-EF1a-DIO-EYFP (AAV2) was prepared by the UNC Viral Core.
600 AAV-DIO-TK-P2A-EGFP and HSV-H129-ΔTK-tdTomato were prepared by the University of
601 California Irvine Viral Core.
602 All AAV viruses were diluted with PBS to a final concentration between 5×10^{12} and $1 \times$
603 10^{13} genome copies per mL before stereotactic delivery into the mouse brain. HSV-H129-ΔTK-
604 tdTomato was administered at 5×10^{8} PFU per mL (100 nL unilaterally).
605
606 **Chemogenetic induction and inhibition of torpor**
607 *Induction*
608 Cre-expressing animals were bilaterally transduced with AAV8-hSyn-DIO-hM3D(Gq)-mCherry.
609 Gq-DREADD-transduced animals were implanted with telemetric temperature probes and
610 allowed to recover for a minimum of 5 days post-surgery. Following this recovery window,
611 animals were injected with CNO, and body temperature was monitored to confirm accuracy of
612 injection. Animals were considered to be torpid if their body temperatures decreased below 34°C
613 upon CNO administration.
614
615 CNO solution was prepared by initially dissolving CNO hydrochloride (Sigma-Aldrich,
616 SML2304) in H_2O to generate a stock solution of 5 mg/mL. The stock solution was diluted with
617 PBS to a final concentration of 0.2 mg/mL, and approximately 125 μL was injected

618 intraperitoneally per mouse for a final injection concentration of 1 mg kg^{-1} in bilaterally injected
619 animals. Unilaterally injected animals received concentrations of 2 mg kg^{-1}.
620
621 *Inhibition*
622 Cre-expressing animals were bilaterally transduced with AAV8-hSyn-DIO-hM4D(Gi)-mCherry.
623 Gi-DREADD-transduced animals were implanted with telemetric temperature probes and
624 allowed to recover for a minimum of 5 days post-surgery. Following this recovery window,
625 animals were first fasted overnight starting in the dark phase (ZT12-12). Animals were injected
626 with PBS at ZT22, right before the onset of the light phase, and body temperature was monitored
627 to confirm accuracy of injection. Animals were considered to be torpid if their body temperatures
628 decreased below 34°C. Animals were recovered for 7 days, and subjected to this fasting
629 paradigm again, except CNO (10 mg/kg) was injected at ZT22. Injections were considered
630 successful if animals entered torpor when injected with PBS, but did not when injected with
631 CNO. If entry into torpor was not inhibited by CNO the animals were excluded from further
632 experiments.
633
634 **Optogenetic stimulation of avPOA^{Vglut2} neurons**
635 Animals expressing either ChR2(H134R) or an EYFP control, and implanted with a fiber optic
636 cannula, were allowed to recover 5 days post-surgery before confirming proper injection location
637 via CNO stimulation. Animals that failed to demonstrate a body temperature decrease were
638 excluded from further analysis. After a 2-week post-surgery recovery period to allow for
639 adequate viral expression, awake, freely moving animals were tethered to a fiber optic patch cord
640 (Doric) and placed in a deep-well cage (WPI) with free access to food and water. Animals were
641 allowed to acclimate to the new environment for 1 h prior to the start of stimulation. To deliver
642 light pulses a PulsePal2 (SanWorks) was utilized as a pulse train generator, which was connected
643 to a desktop computer via USB and controlled via a custom Python script. Pulses from the
644 controller were conveyed via a 455 nm fiber-coupled LED (ThorLabs M455F3) connected to the
645 mouse via patch cords connected through a rotary joint (ThorLabs RJ1) to allow for
646 unencumbered movement of the animal. For ChR2 experiments, the stimulation paradigm was as
647 follows: 8.5 mW, 10 µs pulse, 50 µs interval (16 Hz), Duty Cycle 1s ON 1s OFF. Power output
648 was confirmed at the fiber tip via a power meter (ThorLabs PM100D) prior to each experiment.

649 For fasting experiments, such as GTT or overnight fasting, an identical setup was utilized, but
650 the animal was not given food (access to water was maintained).
651
652 Following the completion of optogenetic experiments, animals were sacrificed, perfused with 4%
653 PFA, and their brains were sectioned to confirm the accuracy of fiber placement.
654
655 **Intraperitoneal glucose tolerance tests (GTT)**
656 For chemogenetic glucose tolerance testing, Gq-DREADD or Gi-DREADD-expressing and
657 control animals were weighed and moved to a clean cage containing a bedding square and water,
658 but no food, prior to the beginning of the dark cycle (ZT 11.5), and placed onto telemetric
659 temperature platforms. After 3 hours of fasting and a "Pre-CNO" blood glucose reading (Bayer
660 Onetouch), animals were injected with 1 mg kg^{-1} CNO and returned to their cage for 60 minutes.
661 A baseline blood glucose reading was subsequently taken (t = 0), and animals were injected with
662 2 g/kg glucose (10*Body Weight 20% glucose). Blood glucose readings were then taken at 15,
663 30, 45, 60, 90, and 120 minutes post-glucose injection prior to returning animals to their home
664 cages.
665
666 For optogenetic glucose tolerance tests, ChR2(H134R)- or EYFP-expressing animals were
667 weighed and connected to a fiber optic patch cord and placed in a clean cage with a nesting
668 square and water but no food. Animals were fasted for 3 hours, sampled for blood, and injected
669 with a volumetrically equivalent amount of saline to CNO that would have been injected in a
670 chemogenetic GTT (i.e. 5 μL saline/g of mouse). After a 60-minute interval, a baseline blood
671 sample was taken, and animals were injected with 2 g/kg glucose. Immediately upon glucose
672 injection, blue light (455 nm) stimulation commenced. Blue light stimulation was continued
673 throughout the duration of the experiment, and blood was sampled at the time points previously
674 described. Blue light stimulation was terminated after t = 120 minutes, and animals were
675 disconnected and returned to their home cages.
676
677 Data were recorded, graphed, and analyzed in GraphPad Prism. AUC calculations were
678 performed using GraphPad Prism analytical tools.
679

680 **Radioactive glucose uptake**

681 *Radioactive glucose uptake assay*

682 Male 8-12-week-old *Vglut2-IRES-Cre* animals were transduced with either mCherry or Gq-
683 DREADD. After validating Gq-DREADD animals' ability to undergo chemogenetic topor,
684 animals were weighed, transferred to a new cage, and fasted for 3 hours. Animals were
685 administered CNO and allowed to equilibrate body temperature for 60 minutes, upon which time
686 initial blood glucose and scintillation counting samples were taken and animals were injected
687 with a mixture of 20 μCi 2-[1,2-^{3}H(N)]-Deoxy-D-glucose (^{3}H-2-DG), 0.5 U/kg Insulin, and 1
688 mM 2-Deoxy-Glucose as per Møller et al[41]. Animals were then placed in a new cage, and 3 μL
689 of blood were taken for scintillation counting along with 1 drop for blood glucose measurements
690 at 5, 10, 20, and 30 minutes post-injection. Blood collected for scintillation counting was added
691 to 5 mL of Opti-Fluor (Perkin-Elmer), mixed, and placed into a Perkin-Elmer Imager for
692 scintillation counting. Following 30-40 minutes of uptake, animals were euthanized, and their
693 gastrocnemius, soleus, and BAT were dissected and snap-frozen in liquid nitrogen. Scintillation
694 samples were measured for tritium over 1 minute, and plasma tritium concentration were
695 recorded as disintegrations per minute (DPM).

696

697 *Determination of tissue-specific glucose uptake rate*

698 To determine tissue-specific glucose uptake rate, we performed chromatographic
699 separation of ^{3}H-2-DG from ^{3}H-2-DG-6-Phosphate, based on a protocol developed by Kim et
700 al[20]. Using ^{3}H-2-DG-6-Phosphate as a proxy for tissue-specific uptake is predicated on the fact
701 that ^{3}H-2-DG is metabolized to ^{3}H-2-DG-6-Phosphate almost immediately upon entry into the
702 cell, which then precludes its exit from the tissue. Measurement of total ^{3}H-2-DG includes
703 interstitial, unmetabolized ^{3}H-2-DG, and is therefore susceptible to artefactual over- or under-
704 estimation of glucose uptake based on state-dependent differences in tissue perfusion. To avoid
705 this confound, we utilized Poly-Prep anion exchange columns (Bio-Rad, 731-6211) to isolate the
706 ^{3}H-2-DG-6-Phosphate. Briefly, tissues were weighed and homogenized in 10 volumes of sterile,
707 deionized water. Homogenized tissues were then heated to 95°C for 10 minutes, cooled to room
708 temperature, vortexed, and centrifuged for 10 minutes at 21430 RCF. Subsequently, 33.3 μL of
709 homogenate was added to 4.967 mL of Opti-Fluor for scintillation counting. During this time,
710 the Poly-Prep anion exchange column was equilibrated with 6 mL of sterile deionized water.

711 Following equilibration, 333 μL of homogenate was applied to the columns and allowed to flow
712 through by gravity. The column was subsequently washed 3 times with 2 mL of sterile,
713 deionized water, and the flowthrough was collected in scintillation vials as the "wash" fraction.
714 Finally, the ^{3}H-2-DG-6-Phosphate was eluted from the column using a 0.3 M Formic Acid/0.5 M
715 NH_4CH_3COO elution buffer. Elution was accomplished via 3 washes of 2 mL using the elution
716 buffer and collected in scintillation vials. The wash and elution (500 μL) were added to 5 mL of
717 Opti-Fluor, and the samples were vortexed and analyzed via scintillation counting.
718
719 For quantitation of tissue-specific glucose uptake rates, we employed a method modified
720 from Møller et al[41]. Briefly, the DPM of the eluate, representing the ^{3}H-2-DG-6-Phosphate
721 concentration in the tissue, was related to the time of uptake and weight of tissue to obtain a
722 DPM g^{-1} min^{-1} value, representing tissue-specific uptake rate. The time-weighted ^{3}H-2-DG
723 appearance was then extrapolated from the DPM of ^{3}H-2-DG in the blood and divided by the
724 time-weighted total glucose concentration to obtain the specific activity of ^{3}H-2-DG in the blood
725 (DPM/μmol). The glucose uptake index for the tissue was then calculated by dividing the tissue
726 uptake rate by the specific activity, and expressing this value as nmol g^{-1} min^{-1}.
727
728 **Immunoblotting**
729 Male, 8-12-week-old *Vglut2-IRES-Cre* animals validated to have body temperature drops and
730 glucose intolerance when stimulated with CNO were subdivided into three cohorts, injected with
731 either saline, CNO (1 mg/kg), or insulin (0.5 IU/kg), respectively, and monitored for blood
732 glucose changes over a 45-minute period. After 45 minutes, animals were sacrificed, and
733 gastrocnemius, soleus, quadriceps, liver, and BAT were dissected and snap-frozen. These tissues
734 were then homogenized in Radioimmunoprecipitation (RIPA) Buffer composed of 150 mM
735 NaCl, 1.0% (w/v) Triton X-100, 0.5% (w/v) Sodium Deoxycholate, 0.1% (w/v) sodium
736 dodecylsulfate, 50 mM Tris (pH 8), EDTA-free protease inhibitor (Roche), and PhosSTOP
737 phosphatase inhibitor (Roche), using a BioRuptor (Qiagen). Lysates were cleared by
738 centrifugation in a microcentrifuge (21430 RCF for 10 min at 4°C), and protein concentrations
739 were quantified using the Pierce BCA Protein Assay Kit (Thermo Fisher). Lysate samples were
740 prepared by the addition of 5× Laemelli Buffer (0.242 M Tris, 10% SDS, 25% glycerol, 0.5 M
741 dithiothreitol (DTT) and bromophenol blue), resolved by Bis-Tris SDS–PAGE, and analyzed by

742 immunoblotting. Antibodies and concentrations used for immunoblotting include Insulin
743 Receptor β (4B8) Rabbit mAb #3025 (Cell Signaling Technologies) 1:1000, Akt Antibody #9272
744 (Cell Signaling Technologies) 1:1000, and Phospho-Akt (Ser473) Antibody #9271 (Cell
745 Signaling Technologies) 1:500. Proteins were visualized using an Anti-rabbit IgG HRP-linked
746 Antibody #7074 (Cell Signaling Technologies) 1:3000 in combination with the
747 chemiluminescent Pierce™ ECL Western Blotting Substrate (ThermoFisher) using an X-OMAT
748 film processor.
749
750 **Sciatic nerve denervation**
751 Sciatic nerve denervation procedures were modeled on those described in Volodin et al[42].
752 Briefly, animals were anesthetized with 3% isoflurane and administered analgesics. The sciatic
753 nerve was then accessed via the back right flank of the animal and severed at both distal and
754 proximal ends, such that there was no reattachment of nerve fibers during the course of recovery.
755 Accuracy of the cut was validated via observation of the animal post-operation. Severing the
756 sciatic nerve causes a stereotyped dragging of the ipsilateral limb. Animals confirmed to have
757 successful denervations were included in experimental cohorts, whereas those that retained limb
758 mobility were excluded. Animals were allowed to recover for 72 hours prior to use in radioactive
759 glucose uptake assays previously described.
760 When dissecting organs for analysis of tissue-specific glucose uptake, both innervated
761 and denervated gastrocnemius muscles were harvested. These tissues were processed in an
762 identical manner, and the ratio of innervated:denervated glucose uptake was used as a metric for
763 the reduction in glucose uptake in the same animal that resulted from denervation.
764
765 **Blood collection**
766 Tail blood was collected from animals by opening a small hole in the tail of the animal
767 and manually extracting 20 μL of blood into a Lithium Heparin Microvette (Sarsdedt). For
768 longitudinal assays, no more than 150 μL of blood was removed from an animal. Following
769 blood extraction, microvettes were placed on ice for no longer than 60 minutes, and then
770 centrifuged in a microcentrifuge for 5 minutes at 2000 RCF to separate blood cells from plasma.
771 Plasma was extracted from these tubes, aliquoted, snap-frozen in liquid N_2, and placed at -80°C
772 for long-term storage.

773

774 **ELISA assays**

775 All assays were performed according to manufacturers' instructions, as briefly described below:

776 *Insulin*

777 Following plasma separation, 10 μL plasma from each mouse was used for the Mouse Ultra-
778 Sensitive ELISA Assay (Crystal Chem), plated in 5 μL duplicates. Samples were compared
779 against a standard curve and analyzed using a Spectramax iD3 plate reader with a reference
780 wavelength of 630 nm and a measured wavelength of 450 nm. Data were fit using a linear curve,
781 and cohort analysis was performed using two-tailed t-tests.

782 *Glucagon*

783 Following plasma separation, 20 μL plasma from each mouse was used for the Mouse Glucagon
784 ELISA Assay (Crystal Chem), plated in 10 μL duplicates. Samples were compared against a
785 standard curve and analyzed using a Spectramax iD3 plate reader with a reference wavelength of
786 630 nm and a measured wavelength of 450 nm. Data were fit using a 4-parameter logistic curve,
787 and cohort analysis was performed using two-tailed t-tests.

788 *Leptin*

789 Following plasma separation, 10 μL plasma from each mouse was used for the Mouse Leptin
790 ELISA Assay (Crystal Chem), plated in 5 μL duplicates. Samples were compared against a
791 standard curve and analyzed using a Spectramax iD3 plate reader with a reference wavelength of
792 630 nm and a measured wavelength of 450 nm. Data were fit using a 4-parameter logistic curve,
793 and cohort analysis was performed using two-tailed t-tests.

794 *Corticosterone*

795 Following plasma separation, 5 μL plasma from each mouse was used for the Corticosterone
796 ELISA Assay (Enzo Life Sciences). Samples were enriched for steroids using the provided
797 Steroid Displacement Reagent and plated in duplicate. Samples were compared against a
798 standard curve and analyzed using a Spectramax iD3 plate reader with a reference wavelength of
799 580 nm and a measured wavelength of 405 nm. Data were fit using a 4-parameter logistic curve,
800 and cohort analysis was performed using two-tailed t-tests.

801

802 **Polar serum metabolomics**

803 To begin, 10 μL aliquots of plasma from blood samples was combined with 90 μL of
804 75:25:0.2 acetonitrile:methanol:formic acid containing 0.2 μg/mL internal standards and
805 vortexed for 5 minutes as 4°C. Subsequently, the samples were spun at 21430 RCF for 10
806 minutes in a refrigerated centrifuge at 4°C. Supernatant was taken, and 15 μL was added to
807 LC/MS vials for analysis.
808 Analysis was conducted on a QExactive benchtop Orbitrap mass spectrometer equipped
809 with an Ion Max source and a HESI II probe, which was coupled to a Dionex UltiMate 3,000
810 UPLC system (Thermo Fisher Scientific). External mass calibration was performed using the
811 standard calibration mixture every 7 days. Chromatographic separation was achieved using the
812 following conditions: buffer A was 20 mM ammonium carbonate, 0.1% ammonium hydroxide;
813 buffer B was acetonitrile. The column oven and autosampler tray were held at 25°C and 4°C,
814 respectively. The chromatographic gradient was run at a flow rate of 0.150 mL min−1 as
815 follows: 0–20 min: linear gradient from 80% to 20% B; 20–20.5 min: linear gradient from 20%
816 to 80% B; 20.5–28 min: hold at 80% B. The mass spectrometer was operated in full-scan,
817 polarity switching mode with the spray voltage set to 3.0 kV, the heated capillary held at 275°C,
818 and the HESI probe held at 350°C. The sheath gas flow was set to 40 units, the auxiliary gas
819 flow was set to 15 units, and the sweep gas flow was set to 1 unit. The data acquisition was
820 performed over a range of 70–1,000 m/z, with the resolution set at 70,000, the automatic gain
821 control target at 10E6, and the maximum injection time at 20 ms. Relative quantitation of polar
822 metabolites was performed with TraceFinder 2.2 (Thermo Fisher Scientific) using a 5 p.p.m.
823 mass tolerance and referencing an in-house library of chemical standards.
824
825 **Hyperinsulinemic-euglycemic clamp**
826 Survival surgery, to place an indwelling intravenous catheter, was performed 5~6 days prior to
827 the insulin clamp experiments[20]. On the day of the euglycemic clamp experiment, mice were
828 placed in a rat restrainer with their tails tape-tethered at one end to minimize animal stress and
829 allow access to tail blood sampling during the experiment. Mice were allowed to acclimatize to
830 this state for 2 hours prior to the insulin infusion. During this 2-h acclimation period, D-[3-^{3}H]
831 glucose was infused (0.05 μCi/min) using a microdialysis pump to assess the basal rate of whole-
832 body glucose turnover (i.e, basal hepatic glucose production). Subsequently, a baseline blood

833 sample (60 μL) was collected for the measurement of basal plasma glucose, insulin, and [^{3}H]
834 glucose concentrations[20].
835 Following the basal period, a 2-h hyperinsulinemic-euglycemic clamp was conducted
836 with a primed (150 mU/kg body weight) and continuous infusion (2.5 mU/kg/min) of human
837 insulin to raise plasma insulin within a physiological range (approximately 300 pM)[20]. Blood
838 samples (10 μL) were collected at 10~20-minute intervals for the measurement of plasma
839 glucose levels. Based on plasma glucose levels, 20% glucose was infused at variable rates to
840 maintain euglycemia (~120 mg/dL) throughout the clamp. To determine insulin-stimulated
841 whole-body glucose turnover, continuous infusion of [3-^{3}H] glucose was applied throughout the
842 clamp (0.1 μCi/min). To estimate insulin-stimulated glucose uptake in individual organs, a bolus
843 of 2-deoxy-d-[1-^{14}C] glucose (2-[^{14}C]DG) (10 μCi) was administered at 75 min after the start of
844 the clamp[20]. Blood samples (10 μL) were taken at 80, 85, 90, 100, 110, and 120 min for the
845 measurement of plasma [^{3}H] glucose, ^3H_2O, and 2-[^{14}C] DG concentrations. A final blood
846 sample (20 μL) was taken at the end of the clamp to measure plasma insulin concentrations.
847 At the end of the insulin clamp, mice were anesthetized, and skeletal muscles (gastrocnemius and
848 quadriceps) from both hindlimbs, white and brown adipose tissues, liver, brain, and heart were
849 collected for biochemical analysis[20]. The tissues were rapidly frozen in liquid N_2, and stored at
850 −80°C until biochemical analysis was performed. Tissue-specific uptake was determined as
851 described in **Radioactive glucose uptake** above.
852
853 **Phosphoproteomics**
854 *Proteolytic digestion and peptide extraction*
855 Tissues were lysed at 70°C for 15 min in 1 mL 1X SDS lysis buffer (5 % (w/v) SDS, 100 mM
856 TEAB pH 8.5, 40 mM CAA, 10 mM TCEP, protease inhibitor cocktail, phosphatase inhibitor
857 cocktail) in Low Protein Binding Microcentrifuge Tubes (Thermo Scientific, Waltham, MA,
858 USA). Cellular debris was removed by centrifugation at 15,000 x g for 5 min. Protein (600 μg)
859 was purified via the SP3 method as in Hughes et al[43]. Proteins were bound to 120 μL SP3 beads
860 by adding 2.4 mL 100 % (v/v) ethanol followed by three washing steps with 1 mL 80 % (v/v)
861 ethanol. Samples were digested with trypsin/LysC mix (1:50) in 300 μL 100 mM TEAB, and
862 proteins were digested overnight in a shaking incubator at 37°C at 115 RPM. The following day,
863 an additional 6 μg trypsin/Lys-C mix was added in 6 μL 100 mM TEAB and the digestion

864 continued for 4 hours at 37°C. Peptide digests (240 µg) were dried in a speed-vac concentrator
865 and resuspended in 40 µL 100 mM TEAB. Peptides were labeled with 500 µg TMTpro label
866 resuspended in 20 µL anhydrous acetonitrile. TMTpro-labeled samples were quenched for 30
867 min at room temperature with 5 µL 5% hydroxylamine in 100 mM TEAB. Labeled peptides
868 were pooled together and desalted on a 500 mg C18 SepPak column (Waters, Milford, MA,
869 USA).
870 The TMTpro pooled sample was split, with one part used for proteome analysis and the other
871 part used for phosphopeptide enrichment. The proteome sample was fractionated using a Strong
872 Anion Exchange column (Thermo Scientific, Waltham, MA, USA). Increasing concentrations of
873 ammonium acetate (0, 20, 50, 100, 200, 500 mM) were used for elution. Low salt fractions (0,
874 20, 50 mM ammonium acetate) and high salt fractions (100, 200, 500 mM ammonium acetate)
875 were pooled, respectively, and lyophilized. The phosphopeptide sample was enriched using the
876 High Select™ TiO_2 phosphopeptide enrichment kit according to the manufacturer's instructions
877 (Thermo Scientific, Waltham, MA, USA). All TiO_2 flowthrough and wash fractions were
878 pooled, lyophilized, and further enriched using the High Select™ Fe-NTA phosphopeptide
879 enrichment kit according to the manufacturer's instructions (Thermo Scientific, Waltham, MA,
880 USA). The low salt and high salt proteome samples, as well as both phosphopeptide-enriched
881 samples, were then fractionated with the High pH Reversed-Phase Peptide Fractionation Kit
882 (Thermo Scientific, Waltham, MA, USA) using the following 12-step gradient of increasing
883 acetonitrile concentrations: 5, 7.5, 10, 12.5, 15, 17.5, 20, 22.5, 25, 27.5, 30, 60%. The following
884 fractions were then pooled together and lyophilized: 1+7, 2+8, 3+9, 4+10, 5+11, 6+12.
885 Lyophilized fractions were resuspended in 12 µL 0.2% formic acid in MS-grade water for LC-
886 MS analysis.
887 *LC-MS data collection:*
888 Mass spectrometry was performed using an Orbitrap Eclipse mass spectrometer equipped with a
889 FAIMS Pro source, connected to a Vanquish Neo nLC chromatography system using an
890 EasySpray ES902 column (75 µm x 25 cm, 100 Å), all from Thermo Fisher Scientific (Waltham,
891 MA, USA). Peptides were separated at 300 nL/min on a gradient of 3–25% B for 90 min, 25–
892 40% B for 30 min, 40–95% B for 10 min, 95% B over 6 min, using 0.1% FA in water for A and
893 0.1% FA in 80% acetonitrile for B. The Orbitrap and FAIMSpro were operated in positive ion
894 mode with a positive ion voltage of 2100 V, an ion transfer tube temperature of 305°C, and a 4.2

895 L/min carrier gas flow, using standard FAIMS resolution and compensation voltages of -45, –55,
896 and –65 V. Full scan spectra were acquired in profile mode at a resolution of 120,000 (MS1 and
897 MS2), with a scan range of 400–1400 m/z, custom maximum fill time (200 ms), custom AGC
898 target (100% MS1, 250% MS2), isolation windows of m/z 0.7, intensity threshold of 2.0e4, 2–6
899 charge state, dynamic exclusion of 60 seconds, and 35% HCD collision energy.
900
901 *Proteomic and Phosphoproteomic Data Analysis*
902 Proteome data were analyzed using the PEAKS Studio 10.6 software package. Raw data
903 extracted from .raw files were pre-processed with the following settings: scans were merged
904 within a 10 ppm retention time window and a 10 ppm precursor m/z tolerance, including
905 precursor mass and charge states (z = 2-8). Pre-processing steps included automatic centroiding,
906 deisotoping, and deconvolution.
907 Protein identification was performed using a mouse protein FASTA database (Uniprot Taxon ID
908 10090), with the following parameters: parent mass error tolerance set to 10 ppm, fragment mass
909 error tolerance set to 0.05 Da, retention time shift tolerance of 5.0 minutes, and semispecific
910 trypsin enzyme specificity. TMT was applied as an unvariable modification, while the variable
911 modifications considered included carbamidomethylation (C), oxidation (M), phosphorylation
912 (P), and deamidation (NQ). Non-specific cleavage at one terminus was allowed, with up to three
913 missed cleavages and a maximum of three variable posttranslational modifications per peptide.
914 The false discovery rate (FDR) was estimated using the decoy-fusion approach, with peptides
915 having an FDR ≤ 1% and a significance threshold of 20 (-10lgP) considered confidently
916 identified. For protein quantification, at least two high abundant peptide signals were selected to
917 calculate raw protein peak areas. The software computed phosphosite data by using the
918 abundances of multiple peptides for each phosphorylation.
919
920
921
922
923
924
925

926 **References**

927 1. Perry, R. J. *et al.* Leptin Mediates a Glucose-Fatty Acid Cycle to Maintain Glucose
928 Homeostasis in Starvation. *Cell* **172**, 234-248.e17 (2018).
929 2. Geiser, F. Metabolic Rate and Body Temperature Reduction During Hibernation and Daily
930 Torpor. *Annual Review of Physiology* **66**, 239–274 (2004).
931 3. Muoio, D. M. Metabolic inflexibility: when mitochondrial indecision leads to metabolic
932 gridlock. *Cell* **159**, 1253–1262 (2014).
933 4. Lee, S.-H., Park, S.-Y. & Choi, C. S. Insulin Resistance: From Mechanisms to Therapeutic
934 Strategies. *Diabetes Metab J* **46**, 15–37 (2022).
935 5. Insulin Resistance Is Accompanied by Increased Fasting Glucagon and Delayed Glucagon
936 Suppression in Individuals With Normal and Impaired Glucose Regulation | Diabetes |
937 American Diabetes Association.
938 https://diabetesjournals.org/diabetes/article/65/11/3473/17158/Insulin-Resistance-Is-
939 Accompanied-by-Increased.
940 6. Coutinho, E. A. *et al.* Activation of SF1 Neurons in the Ventromedial Hypothalamus by
941 DREADD Technology Increases Insulin Sensitivity in Peripheral Tissues. *Diabetes* **66**,
942 2372–2386 (2017).
943 7. Flak, J. N. *et al.* Ventromedial hypothalamic nucleus neuronal subset regulates blood glucose
944 independently of insulin. *J Clin Invest* **130**, 2943–2952.
945 8. Douglass, A. M. *et al.* Neural basis for fasting activation of hypothalamic-pituitary-adrenal
946 axis. *Nature* **620**, 154–162 (2023).
947 9. Herman, J. P. *et al.* Regulation of the hypothalamic-pituitary-adrenocortical stress response.
948 *Compr Physiol* **6**, 603–621 (2016).
949 10. Ambler, M., Hitrec, T. & Pickering, A. Turn it off and on again: characteristics and control
950 of torpor. *Wellcome Open Res* **6**, 313 (2022).
951 11. Hrvatin, S., Sun, S., Wilcox, O. F., Yao, H., Lavin-Peter, A. J., Cicconet, M., Assad, E. G.,
952 Palmer, M. E., Aronson, S., Banks, A. S., Griffith, E. C., & Greenberg, M. E. (2020).
953 Neurons that regulate mouse torpor. *Nature*, *583*(7814), 115–121.
954 https://doi.org/10.1038/s41586-020-2387-5

955

956 12.Takahashi, T. M. *et al.* A discrete neuronal circuit induces a hibernation-like state in rodents.
957 *Nature* **583**, 109–114 (2020).
958 13. Yu, S. *et al.* Glutamatergic Preoptic Area Neurons That Express Leptin Receptors Drive
959 Temperature-Dependent Body Weight Homeostasis. *The Journal of Neuroscience* **36**, 5034
960 (2016).
961 14. Wang, Y. & Wu, R. The Effect of Fasting on Human Metabolism and Psychological Health.
962 *Dis Markers* **2022**, 5653739 (2022).
963 15. Roth, B. L. DREADDs for Neuroscientists. *Neuron* **89**, 683–694 (2016).
964 16. Frayn, K. N. Calculation of substrate oxidation rates in vivo from gaseous exchange. *Journal*
965 *of Applied Physiology* **55**, 628–634 (1983).
966 17. Boucher, J., Kleinridders, A. & Kahn, C. R. Insulin Receptor Signaling in Normal and
967 Insulin-Resistant States. *Cold Spring Harbor Perspectives in Biology* **6**, a009191 (2014).
968 18. Leto, D. & Saltiel, A. R. Regulation of glucose transport by insulin: traffic control of
969 GLUT4. *Nat Rev Mol Cell Biol* **13**, 383–396 (2012).
970 19. DeFronzo, R. A., Tobin, J. D. & Andres, R. Glucose clamp technique: a method for
971 quantifying insulin secretion and resistance. *Am J Physiol* **237**, E214-223 (1979).
972 20. Kim, J. K. Hyperinsulinemic–Euglycemic Clamp to Assess Insulin Sensitivity In Vivo. in
973 *Type 2 Diabetes: Methods and Protocols* (ed. Stocker, C.) 221–238 (Humana Press, Totowa,
974 NJ, 2009). doi:10.1007/978-1-59745-448-3_15.
975 21. DeFronzo, R. A. & Tripathy, D. Skeletal Muscle Insulin Resistance Is the Primary Defect in
976 Type 2 Diabetes. *Diabetes Care* **32**, S157–S163 (2009).
977 22. Rudolf, R., Kettelhut, I. C. & Navegantes, L. C. C. Sympathetic innervation in skeletal
978 muscle and its role at the neuromuscular junction. *J Muscle Res Cell Motil* **45**, 79–86 (2024).
979 23. Kalinovich, A. *et al.* Treatment with a β-2-adrenoceptor agonist stimulates glucose uptake in
980 skeletal muscle and improves glucose homeostasis, insulin resistance and hepatic steatosis in
981 mice with diet-induced obesity. *Diabetologia* **63**, 1603–1615 (2020).
982 24. Navegantes, L. C., Resano, N. M., Migliorini, R. H. & Kettelhut, I. C. Effect of
983 guanethidine-induced adrenergic blockade on the different proteolytic systems in rat skeletal
984 muscle. *Am J Physiol* **277**, E883-889 (1999).
985 25. Megeney, L. A. *et al.* Regulation of muscle glucose transport and GLUT-4 by nerve-derived
986 factors and activity-related processes. *Am J Physiol* **269**, R1148-1153 (1995).

987 26. Marinelli, M., Rougé-Pont, F., De Jesus-Oliveira, C., Le Moal, M. & Piazza, P. V. Acute
988 blockade of corticosterone secretion decreases the psychomotor stimulant effects of cocaine.
989 *Neuropsychopharmacology* **16**, 156–161 (1997).
990 27. Yang, H. *et al.* A novel H129-based anterograde monosynaptic tracer exhibits features of
991 strong labeling intensity, high tracing efficiency, and reduced retrograde labeling. *Mol*
992 *Neurodegener* **17**, 6 (2022).
993 28. Kataoka, N., Hioki, H., Kaneko, T. & Nakamura, K. Psychological Stress Activates a
994 Dorsomedial Hypothalamus-Medullary Raphe Circuit Driving Brown Adipose Tissue
995 Thermogenesis and Hyperthermia. *Cell Metabolism* **20**, 346–358 (2014).
996 29. Madden, C. J. & Morrison, S. F. Excitatory amino acid receptor activation in the raphe
997 pallidus area mediates prostaglandin-evoked thermogenesis. *Neuroscience* **122**, 5–15 (2003).
998 30. Moffitt, J. R. *et al.* Molecular, spatial, and functional single-cell profiling of the
999 hypothalamic preoptic region. *Science* **362**, eaau5324 (2018).
1000 31. Tan, C. L. *et al.* Warm-Sensitive Neurons that Control Body Temperature. *Cell* **167**, 47-
1001 59.e15 (2016).
1002 32. Roh, E., Song, D. K. & Kim, M.-S. Emerging role of the brain in the homeostatic regulation
1003 of energy and glucose metabolism. *Exp Mol Med* **48**, e216–e216 (2016).
1004 33. Lee, ML., Chang, CP., Toda, C. *et al.* Body temperature regulates glucose metabolism and
1005 torpid behavior. *Nat Commun* **16**, 6278 (2025). https://doi.org/10.1038/s41467-025-61499-2
1006 34. Rubio, W. B., Cortopassi, M. D., Ramachandran, D., Walker, S. J., Balough, E. M., Wang, J.,
1007 & Banks, A. S. (2023). Not so fast: Paradoxically increased variability in the glucose
1008 tolerance test due to food withdrawal in continuous glucose-monitored mice. *Molecular*
1009 *metabolism*, *77*, 101795. https://doi.org/10.1016/j.molmet.2023.101795
1010 35. Deem, J. D. *et al.* Warm Responsive Neurons in the Hypothalamic Preoptic Area are Potent
1011 Regulators of Glucose Homeostasis in Male Mice. *Endocrinology* **164**, bqad074 (2023).
1012 36. Allen, W. E. *et al.* Thirst-associated preoptic neurons encode an aversive motivational drive.
1013 *Science* **357**, 1149–1155 (2017).
1014 37. Dagogo-Jack, S. Leptin and Insulin Sensitivity: Endogenous Signals of Metabolic
1015 Homeostasis. *The Journal of Clinical Endocrinology & Metabolism* **109**, e1402–e1403
1016 (2024).

38. Shimogori, T., Abe, A., Go, Y., Hashikawa, T., Kishi, N., Kikuchi, S. S., Kita, Y., Niimi, K., Nishibe, H., Okuno, M., Saga, K., Sakurai, M., Sato, M., Serizawa, T., Suzuki, S., Takahashi, E., Tanaka, M., Tatsumoto, S., Toki, M., U, M., … Okano, H. (2018). Digital gene atlas of neonate common marmoset brain. *Neuroscience research*, *128*, 1–13. https://doi.org/10.1016/j.neures.2017.10.009

39. Kita, Y., Nishibe, H., Wang, Y., Hashikawa, T., Kikuchi, S. S., U, M., Yoshida, A. C., Yoshida, C., Kawase, T., Ishii, S., Skibbe, H., & Shimogori, T. (2021). Cellular-resolution gene expression profiling in the neonatal marmoset brain reveals dynamic species- and region-specific differences. *Proceedings of the National Academy of Sciences of the United States of America*, *118*(18), e2020125118. https://doi.org/10.1073/pnas.2020125118

40. Weir J. B. (1949). New methods for calculating metabolic rate with special reference to protein metabolism. *The Journal of physiology*, *109*(1-2), 1–9. https://doi.org/10.1113/jphysiol.1949.sp004363

41. Møller, L. L. V., Raun, S. H., Fritzen, A. M., & Sylow, L. (2022). Measurement of skeletal muscle glucose uptake in mice in response to acute treadmill running. *Journal of biological methods*, *9*(3), e162. https://doi.org/10.14440/jbm.2022.385

42. Volodin, A., Kosti, I., Goldberg, A. L., & Cohen, S. (2017). Myofibril breakdown during atrophy is a delayed response requiring the transcription factor PAX4 and desmin depolymerization. *Proceedings of the National Academy of Sciences of the United States of America*, *114*(8), E1375–E1384. https://doi.org/10.1073/pnas.1612988114

43. Hughes, C. S., Moggridge, S., Müller, T., Sorensen, P. H., Morin, G. B., & Krijgsveld, J. (2019). Single-pot, solid-phase-enhanced sample preparation for proteomics experiments. *Nature protocols*, *14*(1), 68–85. https://doi.org/10.1038/s41596-018-0082-x

Acknowledgements: We thank T. Diefenbach for his help with whole brain imaging experiments. We thank all Hrvatin Lab members for their insightful comments on the manuscript. Whole brain imaging was performed at the Ragon Institute Microscopy Core. Metabolomics experiments were performed with the Whitehead Institute Metabolomics Core. Proteomic and phosphoproteomics experiments were performed with the Whitehead Institute Quantitative Proteomics Core. Metabolic cage experiments were performed at the BIDMC Energy Balance Core. Metabolic clamp experiments were performed at the UMass Metabolic Disease Research Center.

Funding:

Mathers Foundation Grant (S.H.)
Searle Scholars Program (S.H.)
Pew Charitable Trust (S.H.)
Rosenkranz Foundation (S.H.)
MIT Research Support Committee Grant (S.H.)
Howard Hughes Medical Institute Hrabowski Scholar (S.H.)

Author Contributions:

J.M.R and S.H conceptualized the project. J.M.R, S.H., E.C.G, J.K.K, F.S, and A.S.B devised experimental methodologies. J.M.R, M.A, N.N, H.W, M.M, M.W, B.L, B-Y.K, and B.K executed experiments. J.M.R, S.H, M.A, N.N, and H.W contributed to data visualization. S.H and E.C.G acquired funding. S.H and E.C.G administered and supervised the project. J.M.R, S.H, and E.C.G wrote the initial manuscript draft. J.M.R, S.H, E.C.G, M.A, N.N, H.W, A.S.B, and J.K.K reviewed and edited the manuscript.

Competing Interests:

The authors declare they have no competing interests

Data and Material Availability:

All data needed to evaluate conclusions made in both main text and supplementary figures in this paper will be made available upon reasonable request.

Supplementary Materials

Materials and Methods

Figs S1 to S7

Figures

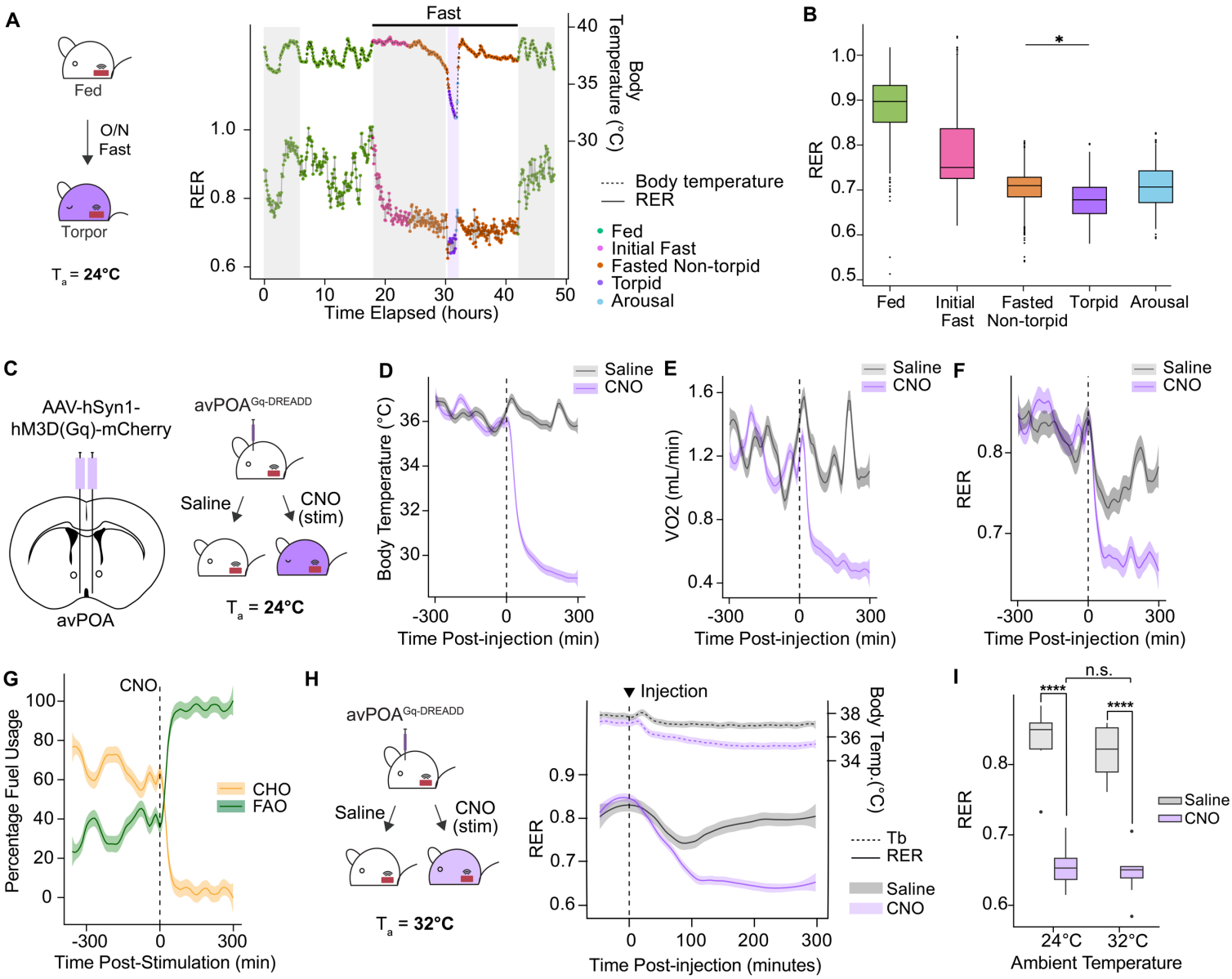

1086 **Figure 1: avPOA^{Vglut2} neurons regulate fuel usage in natural and induced torpor. (A)** *(Left)*
1087 Schematic for respirometry experiments involving natural torpor. Probe-implanted wild-type
1088 C57Bl6/J mice were monitored throughout a 24-hour fast (ZT12-ZT12, denoted by horizontal
1089 line). (*Right)* Representative traces of respiratory exchange ratio (RER, bottom, solid line) and

1090 body temperature (T_b, top, dashed line) for an animal undergoing natural fasting-induced torpor.
1091 Traces were classified into distinct states based on food availability and T_b: *Fed*, ad libitum
1092 access to chow; *Initial Fast*, <6 h post-food withdrawal; *Fasted Non-torpid*, >6 h fasting and T_b >
1093 34.5°C; Torpid –fasted, T_b < 34.5°C, and ΔT_b < 0; *Arousal*, T_b < 35.5°C and ΔT_b > 0. Shaded
1094 gray portions denote dark cycle times (ZT12-24). **(B)** State-dependent quantification of RER for
1095 fasted mice as in (A) (n = 8 animals, 4 male, 4 female, * = $p < 0.05$). **(C)** (*Left)* Schematic for
1096 bilateral stereotactic transduction of avPOA neurons with Gq-DREADD. ***(Right)*** Experimental
1097 paradigm for stimulating avPOA-transduced animals with either saline or CNO (1 mg/kg) at T_a =
1098 24°C. (**D-F)** Quantification of T_b (**D**), VO_2 (**E**), and RER (**F**) in Gq-DREADD-expressing mice
1099 for 300 minutes pre- and post-CNO stimulation (dashed vertical line). Traces and shading
1100 indicate mean ± SEM (n = 8 animals). **(G)** Calculation of carbohydrate oxidation (CHO) and
1101 fatty acid oxidation (FAO) percentages for 300 minutes pre- and post-CNO injection (dashed
1102 vertical line) based on the method of Frayn (see Methods). **(H)** (*Left*) Following acclimation at
1103 elevated T_a (32°C), Gq-DREADD-expressing mice were administered either saline or CNO and
1104 monitored for gas exchange and T_b. (*Right)* RER and T_b changes in Gq-DREADD-expressing
1105 mice in response to CNO stimulation or saline control. Dashed vertical line indicates timing of
1106 the injection. Ambient temperature denoted by horizontal dashed line (T_a = 32°C). **(I)**
1107 Quantitation of RER 300 min following CNO or saline control injections at T_a = 24°C or 32°C
1108 (**** = $p < 0.00005$, n = 8 mice).

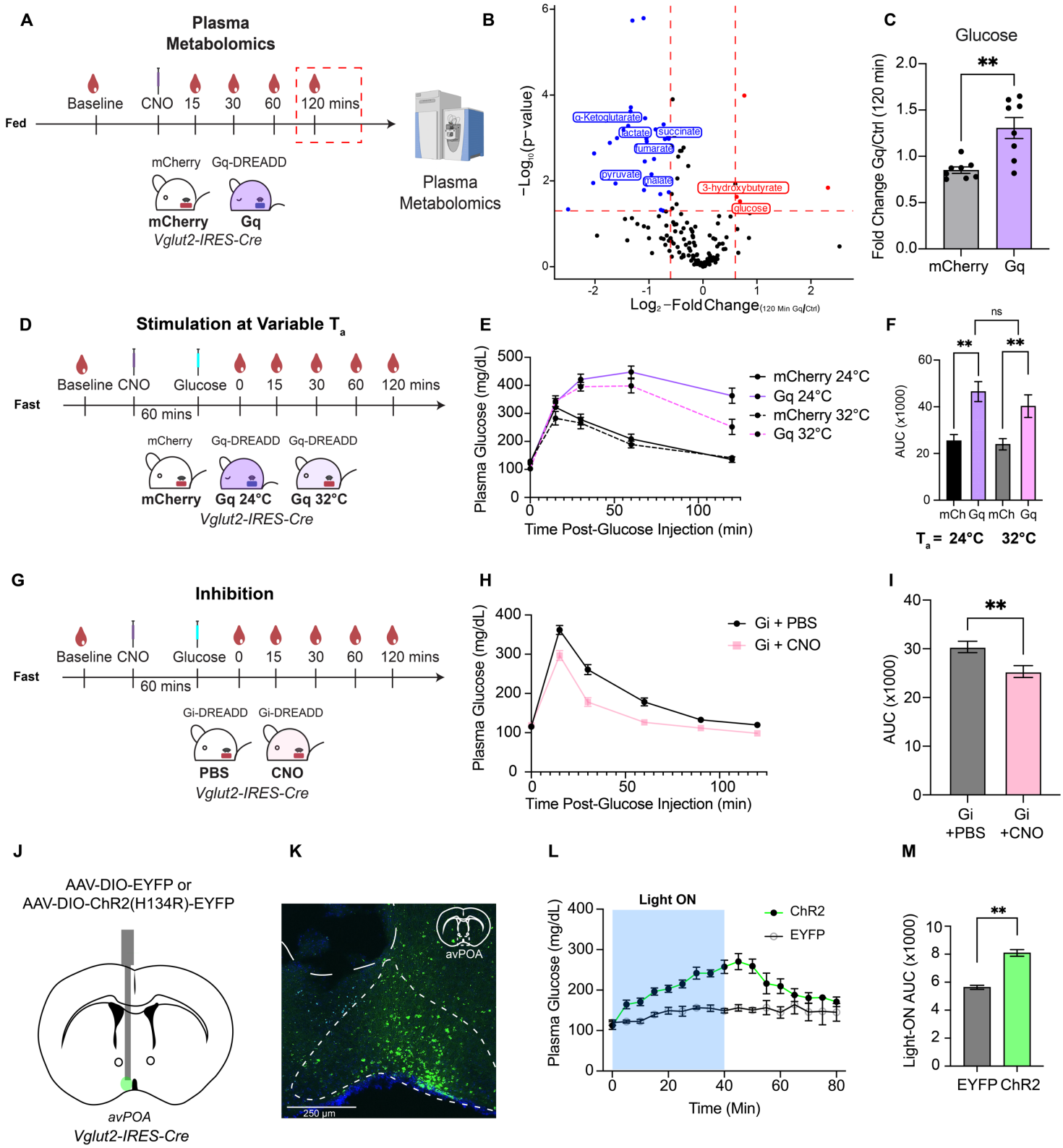

Figure 2: avPOA^{Vglut2} neuronal regulation of whole-body glucose homeostasis is rapid and reversible. (A) Schematic of blood sampling protocol for plasma metabolomics from mCherry-

1111 and Gq-DREADD-transduced *Vglut2-IRES-Cre* mice pre- and post-CNO administration. n = 8
1112 mice (4 female, 4 male) per cohort. Blood samples were taken 0, 15, 30, 60, and 120 min post-
1113 CNO injection (1 mg/kg) for plasma separation, LC/MS, and polar metabolomics analysis. **(B)**
1114 (*Left*) Volcano plot of differentially altered metabolites 120 min post-CNO administration.
1115 Selected overrepresented and underrepresented metabolites labeled in red and blue, respectively.
1116 p-values calculated using two-tailed t-test, red lines corresponding to FDR-corrected $p < 0.05$,
1117 and $|Log_2\text{-Fold change}| > 0.6$. **(C)** Fold-change in glucose abundance in Gq-DREADD-
1118 expressing vs. mCherry control mice at 120 min post-CNO injection. (n = 8 animals, mean
1119 ±SEM, ** = $p<0.005$, two-tailed t-test). **(D)** Schematic for intraperitoneal glucose tolerance test
1120 (GTT) in Gq-DREADD and mCherry control mice. Animals were fasted for 3h prior to baseline
1121 glucose measurement and CNO administration. Subsequent to a 60-minute interval following
1122 CNO administration, a baseline blood sample was taken, animals were injected with glucose (2
1123 g/kg), and subsequent blood samples for changes in glucose levels were obtained at 15, 30, 60,
1124 and 120 min post glucose administration. **(E)** Glucose tolerance testing of mCherry (Ctrl) or Gq-
1125 DREADD-expressing animals at T_a = 24°C or 32°C (24°C: n = 13 mCherry, n = 14 Gq; 32°C: n
1126 = 14 mCherry, n=16 Gq *Vglut2-IRES-Cre* animals, mean ±SEM). **(F)** Area under the curve
1127 (AUC) quantification of (E) in all cohorts (** = $p < 0.005$, student's two-tailed t-test, mean
1128 ±SEM). **(G)** Schematic for GTT in Gi-DREADD-transduced *Vglut2-IRES-Cre* animals. Gi-
1129 DREADD-expressing animals were injected with either PBS or CNO (10 mg/kg) prior to GTT,
1130 and blood was collected as in other GTT experiments. **(H)** Glucose tolerance testing of PBS- and
1131 CNO-injected Gi-DREADD animals (n = 8 PBS, n = 8 CNO, mean ±SEM). **(I)** AUC
1132 quantification of GTT in (H) for PBS- and CNO-injected experiments (** = $p < 0.005$, student's
1133 paired two-tailed t-test, mean ±SEM). **(J)** Schematic of unilateral stereotactic administration of
1134 AAV-DIO-ChR2(H134R)-EYFP or AAV-DIO-EYFP to the avPOA of *Vglut2-IRES-Cre* mice
1135 (n=4 EYFP, n= 5 ChR2). **(K)** Representative image of (J), showing ChR2-EYFP signal in an
1136 experimental animal (Scale bar = 250 μm). **(L)** Plasma glucose sampling of ChR2- and EYFP-
1137 expressing mice for 80 min at 5 min intervals (Light ON 0-40 minutes, indicated by blue
1138 shading; Light OFF 41-80 minutes, indicated by no shading, mean ±SEM). **(M)** AUC
1139 quantification of (L) (** = $p < 0.005$, Students two-tailed t-test, n = 4 EYFP, n = 5 ChR2 *Vglut2-*
1140 *IRES-Cre* animals).

1141

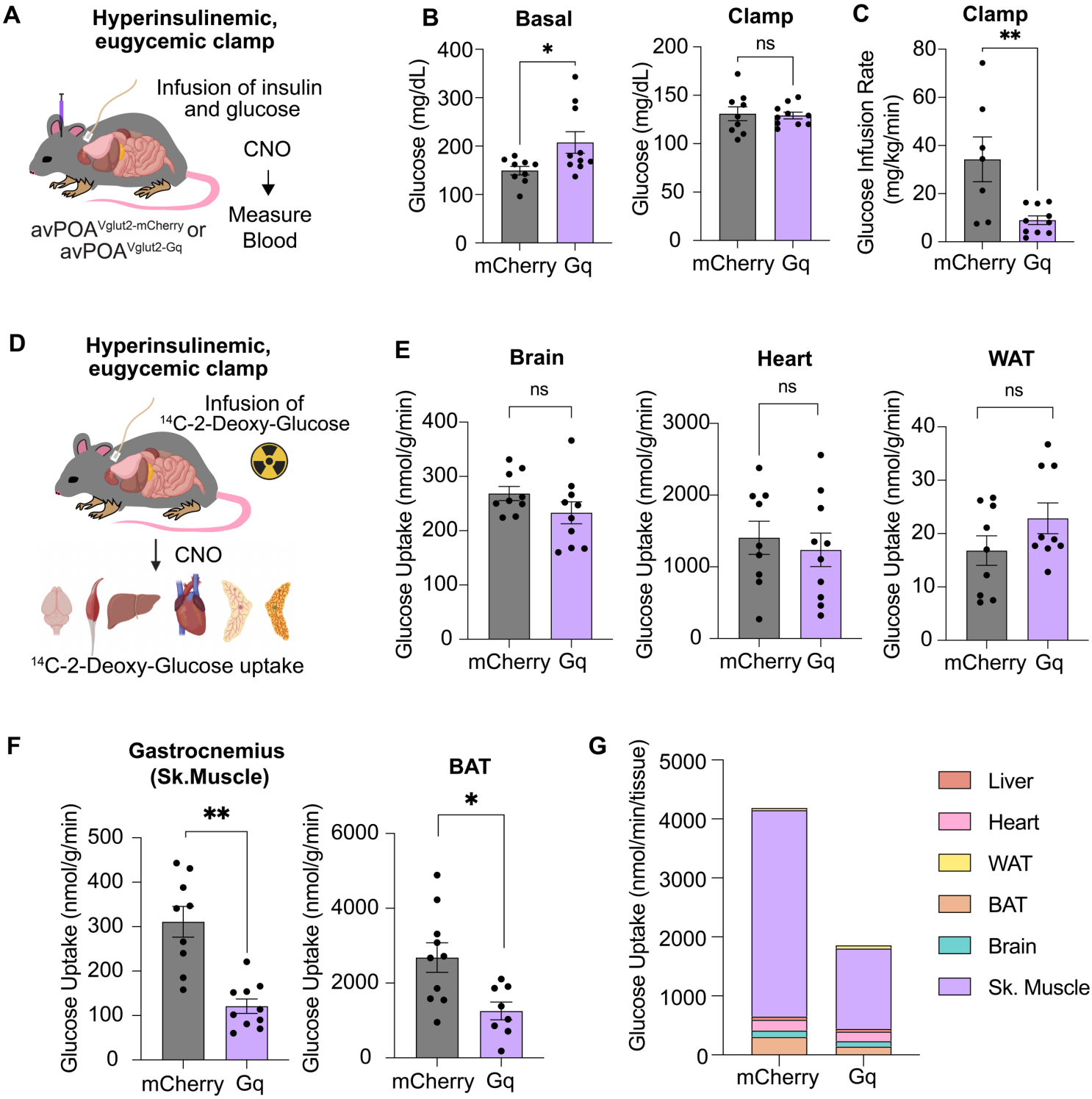
A
Hyperinsulinemic, eugycemic clamp
Infusion of insulin and glucose
CNO
Measure Blood
avPOA Vglut2-mCherry or avPOA Vglut2-Gq
B
Basal
Glucose (mg/dL)
400
300
200
100
0
*
mCherry Gq
Clamp
Glucose (mg/dL)
200
150
100
50
0
ns
mCherry Gq
C
Clamp
Glucose Infusion Rate (mg/kg/min)
80
60
40
20
0
**
mCherry Gq
D
Hyperinsulinemic, eugycemic clamp
Infusion of 14C-2-Deoxy-Glucose
CNO
14C-2-Deoxy-Glucose uptake
E
Brain
Glucose Uptake (nmol/g/min)
400
300
200
100
0
ns
mCherry Gq
Heart
Glucose Uptake (nmol/g/min)
3000
2000
1000
0
ns
mCherry Gq
WAT
Glucose Uptake (nmol/g/min)
40
30
20
10
0
ns
mCherry Gq
F
Gastrocnemius (Sk.Muscle)
Glucose Uptake (nmol/g/min)
500
400
300
200
100
0
**
mCherry Gq
BAT
Glucose Uptake (nmol/g/min)
6000
4000
2000
0
*
mCherry Gq
G
Glucose Uptake (nmol/min/tissue)
5000
4000
3000
2000
1000
0
mCherry
Gq
Liver
Heart
WAT
BAT
Brain
Sk. Muscle

1142 **Figure 3: avPOA ^{Vglut2} neurons coordinate whole-body glucose hypometabolism and organ-**
1143 **specific defects in glucose uptake. (A)** Schematic for hyperinsulinemic-euglycemic clamp and
1144 tissue-specific glucose uptake measurements. Gq-DREADD- or mCherry-transduced animals
1145 were implanted with indwelling catheters, mildly restrained, and subjected to continuous
1146 infusion of glucose, insulin, ^{3}H-glucose, and ^{14}C-2-deoxyglucose over the course of the two-hour
1147 experiment. Glucose levels were maintained at approximately 120 mg/dL to ensure clamp
1148 effectiveness. Animals were sacrificed, and the displayed tissues were taken for radioactive ^{14}C-
1149 2-Deoxyglucose-6-Phosphate uptake analysis. **(B)** Glucose levels 60 min after CNO stimulation
1150 (Basal) were significantly elevated in Gq-DREADD-expressing animals as compared to control
1151 animals (* = $p<0.05$, student's two-tailed t-test, mCherry = 149.4 ± 8.8 mg/dL; Gq = 207.5 ±
1152 22.2 mg/dL, mean ±SEM, n= 9 mCherry, n=10 Gq *Vglut2-IRES-Cre* animals). Conversely,
1153 during the hyperinsulinemic clamp, Gq-DREADD- and mCherry-expressing animals maintained
1154 nearly identical levels plasma glucose (Gq: 130.9 ± 7.2 mg/dL, mCherry: 129.1 ± 3.4 mg/dL),
1155 indicating successful clamping of plasma glucose. **(C)** Glucose Infusion Rate (GIR) of control
1156 (mCherry) and Gq-DREADD-transduced animals throughout the 120-minute duration of the
1157 experiment (** = $p < 0.005$, student's two-tailed t-test, mean ±SEM). **(D)** Organs in which
1158 avPOA stimulation had no significant effect on insulin-stimulated glucose uptake (ns = $p > 0.05$,
1159 student's two-tailed t-test, mean ±SEM). **(E)** Gastrocnemius and BAT exhibited reductions of
1160 61.1% and 55.3% in ^{14}C-2-DG-6-Phosphate uptake (Glucose Uptake), respectively, between Gq-
1161 DREADD- and mCherry-expressing animals (* = $p < 0.05$, ** = $p< 0.005$, student's two-tailed t-
1162 test, mean ±SEM). **(F)** Calculated mass-dependent glucose uptake in each of the six examined
1163 organs based on average tissue weights of control and Gq-DREADD-expressing animals and
1164 tissue-specific glucose uptake rates (Mass-Dependent Uptake (nmol/min) = Average Tissue
1165 Mass (g) * Glucose Uptake Rate (nmol/min/g tissue)).

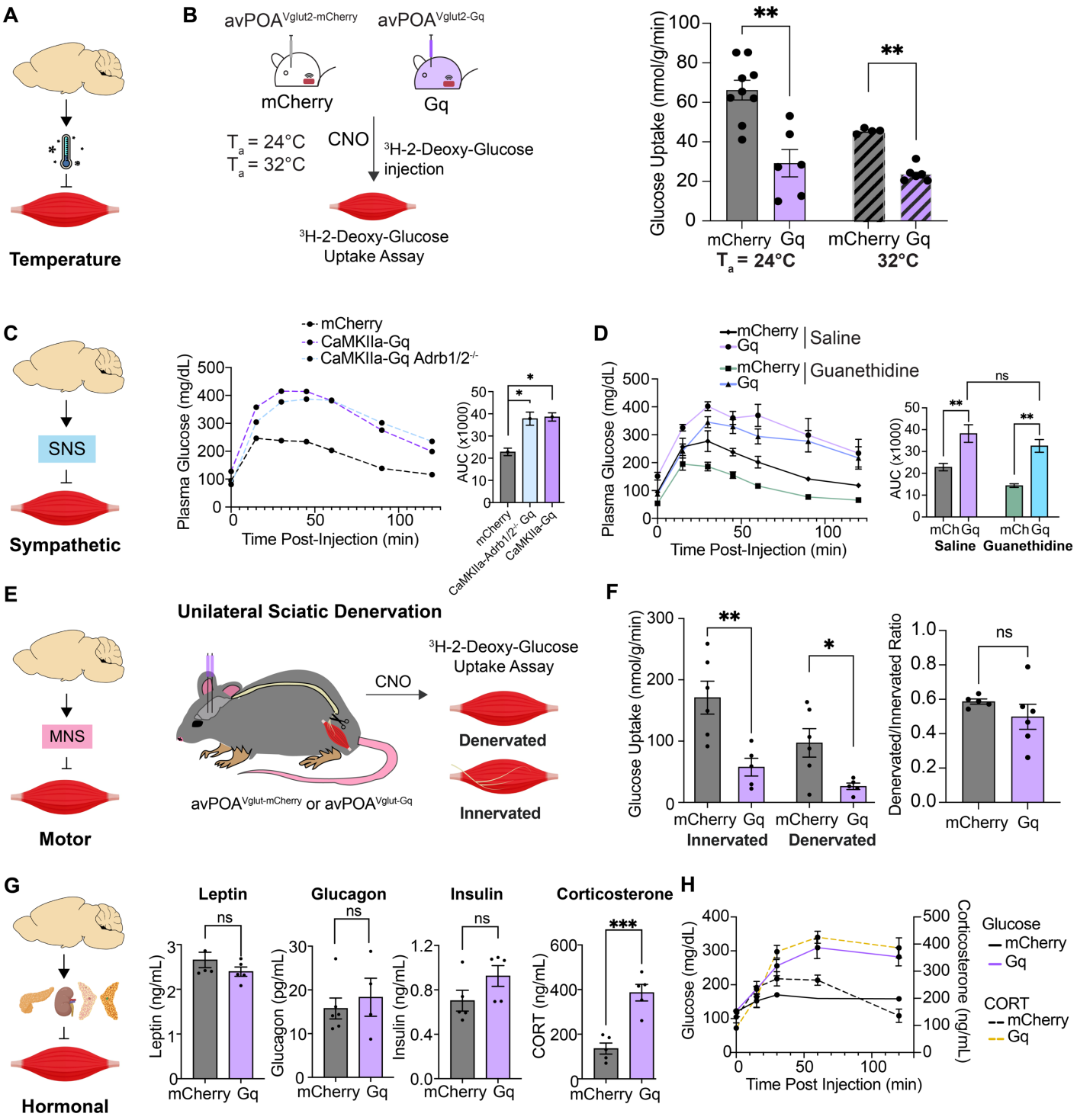
A
Temperature
B
avPOA Vglut2-mCherry
avPOA Vglut2-Gq
mCherry
Gq
Ta = 24°C
Ta = 32°C
CNO
3H-2-Deoxy-Glucose injection
3H-2-Deoxy-Glucose Uptake Assay
Glucose Uptake (nmol/g/min)
mCherry Gq
Ta = 24°C
mCherry Gq
32°C
C
SNS
Sympathetic
mCherry
CaMKIIa-Gq
CaMKIIa-Gq Adrb1/2-/-
Plasma Glucose (mg/dL)
Time Post-Injection (min)
AUC (x1000)
mCherry
CaMKIIa-Adrb1/2-/- Gq
CaMKIIa-Gq
D
mCherry
Gq
Saline
mCherry
Gq
Guanethidine
Plasma Glucose (mg/dL)
Time Post-Injection (min)
AUC (x1000)
ns
mCh Gq
Saline
mCh Gq
Guanethidine
E
MNS
Motor
Unilateral Sciatic Denervation
CNO
3H-2-Deoxy-Glucose Uptake Assay
avPOA Vglut-mCherry or avPOA Vglut-Gq
Denervated
Innervated
F
Glucose Uptake (nmol/g/min)
mCherry Gq
Innervated
mCherry Gq
Denervated
Denervated/Innervated Ratio
ns
mCherry Gq
G
Hormonal
Leptin
Glucagon
Insulin
Corticosterone
ns
ns
ns
Leptin (ng/mL)
Glucagon (pg/mL)
Insulin (ng/mL)
CORT (ng/mL)
mCherry Gq
H
Glucose (mg/dL)
Corticosterone (ng/mL)
Time Post Injection (min)
Glucose
mCherry
Gq
CORT
mCherry
Gq

1166 **Figure 4: Determination of peripheral effectors of avPOA^{Vglut2}-induced skeletal muscle**
1167 **insulin resistance. (A)** Schematic for potential temperature-regulated effects of avPOA^{Vglut2}
1168 neuronal stimulation on skeletal muscle glucose uptake. **(B)** (*Left*) Schematic for radioactive
1169 glucose (^{3}H-2-deoxyglucose-6 phosphate) uptake assay in *Vglut2-IRES-Cre* animals injected
1170 with either Cre-dependent mCherry (avPOA$^{Vglut2-mCherry}$) or Gq-DREADD (avPOA$^{Vglut2-Gq}$), then
1171 pretreated with CNO and subjected to radioactive glucose uptake assay at T_a = 24°C or 32°C.
1172 (*Right)* results of Radioactive glucose (^{3}H-2-deoxyglucose-6 phosphate) uptake assay in
1173 gastrocnemius muscles of control (avPOA$^{Vglut2-mCherry}$) or Gq-DREADD (avPOA$^{Vglut2-Gq}$) mice
1174 housed at T_a =24°C or 32°C (** = $p < 0.005$, student's two-tailed t-test, mean ±SEM, n = 9
1175 mCherry 24°C , n = 6 Gq 24°C, n = 4 mCherry 32°C, n=6 Gq 32°C *Vglut2-IRES-Cre* animals).
1176 **(C)** Glucose tolerance testing of control mCherry-expressing mice (mCherry), mice transduced
1177 with AAV-CaMKIIa-hM3D(Gq)-mCherry (CaMKIIa-Gq), and CaMKIIa-Gq-transduced
1178 *Adrb1/2$^{-/-}$* mice (CaMKIIa-Gq Adrb1/2$^{-/-}$). AUC calculation shown on right (* = $p < 0.05$,
1179 student's two-tailed t-test, mean ±SEM, n = 6 Vglut-mCherry, n = 6 CaMKIIa-Gq, n = 4
1180 CaMKIIa-Gq Adrb1/2$^{-/-}$ animals). **(D)** Pair-matched glucose tolerance tests in animals injected
1181 with saline, CNO (1 mg/kg), Guanethidine (50 mg/kg), or Guanethidine and CNO (ns = $p > 0.05$,
1182 ** = $p < 0.005$, paired student's two-tailed t-test, mean ±SEM, n = 6 mice per condition). **(E)**
1183 Schematic of sciatic nerve denervation paradigm to test the requirement for motor innervation
1184 for avPOA-induced skeletal muscle insulin resistance. Unilateral denervation allows for a
1185 matched innervated internal control. **(F)** Radioactive glucose uptake assay in innervated or
1186 denervated gastrocnemius muscle in CNO-treated control mCherry- and Gq-DREADD-
1187 expressing animals (mCherry innervated = 171.0±26.9, Gq innervated = 57.6±14.5, mCherry
1188 denervated = 97.1±23.2, Gq denervated = 26.3±5.3 nmol/g/min). (*Right*) Ratio of
1189 denervated:innervated gastrocnemius glucose uptake in mCherry animals (59.9±1.5%) and Gq
1190 animals (49.0±7.3%). **(G)** Concentrations of plasma leptin, glucagon, insulin, and corticosterone
1191 60 minutes following CNO administration in fed mCherry- and Gq-DREADD-expressing
1192 animals. (Leptin: n = 5 mCherry, n = 5 Gq; Glucagon: n= 5 mCherry, n = 6 Gq; Insulin: n = 5
1193 mCherry, n = 5 Gq; Corticosterone: n = 5 mCherry, n = 7 Gq animals, ** = $p < 0.005$). **(H)**
1194 Longitudinal monitoring of glucose and corticosterone in fed mCherry- and Gq-expressing mice
1195 injected with 1 mg/kg CNO. Blood plasma taken 0, 15, 30, 60, and 120 minutes post-injection (n
1196 = 7 Gq, n = 5 mCherry *Vglut2-IRES-Cre* animals).

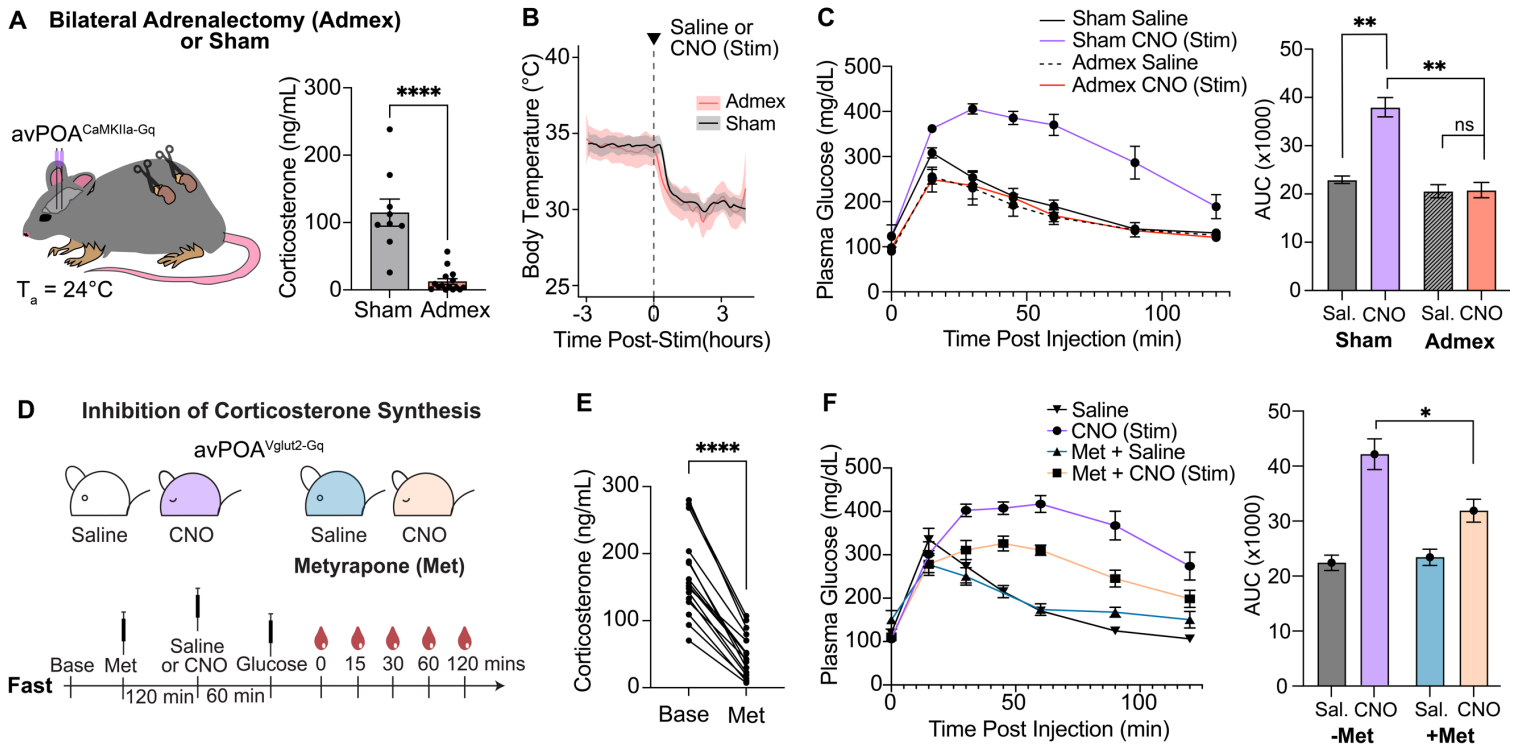

Figure 5: avPOA-induced insulin intolerance requires adrenal hormones. (A) (*Left)* Schematic depicting the use of bilateral adrenalectomized mice (Admex) or sham surgery controls (Sham) stereotactically administered AAV-CaMKIIa-hM3D(Gq). (*Right*) ELISA analysis of plasma corticosterone confirms successful adrenalectomy (**** = $p < 0.00005$, student's two-tailed t-test, mean ±SEM, n = 9 Sham, n = 15 Admex animals). **(B)** Body temperature changes in response to 1 mg/kg CNO in both Sham and Admex animals transduced with AAV-CaMKIIa-hM3D(Gq) (Min T_b Sham = 30.0±0.8°C, Min T_b Admex = 29.5±1.0°C, n= 5 Sham, n=7 Admex animals). Vertical line corresponds to CNO injection. **(C)** Glucose tolerance test of Sham and Admex animals injected with either saline or CNO. AUC quantitation shown on right (** = $p < 0.005$, student's two-tailed t-test, mean ±SEM, n = 5 Sham, n = 7 Admex). **(D)** Schematic for metyrapone treatment during glucose tolerance testing. Animals were fasted for 120 minutes before baseline blood glucose levels were taken. Animals were then injected with 50 mg/kg metyrapone, and CNO was administered 2 hours following metyrapone injection. Subsequently, the GTT proceeded as previously described. **(E)** Corticosterone ELISA on blood sampled from animals prior to metyrapone injection (Base) or 2 hours post-injection (Met) (**** = $p<0.00005$, student's two-tailed t-test, mean ±SEM, n = 6 samples per condition). **(F)** Glucose

1213 tolerance test of Gq-DREADD-transduced *Vglut2-IRES-Cre* animals injected with saline, CNO
1214 (1 mg/kg), saline + metyrapone (50 mg/kg), or CNO (1 mg/kg) + metyrapone (50 mg/kg).
1215 (*Right*) AUC quantitation of results (* = $p < 0.05$, student's two=tailed t-test, mean ±SEM, n = 6
1216 *Vglut2-IRES-Cre* animals).

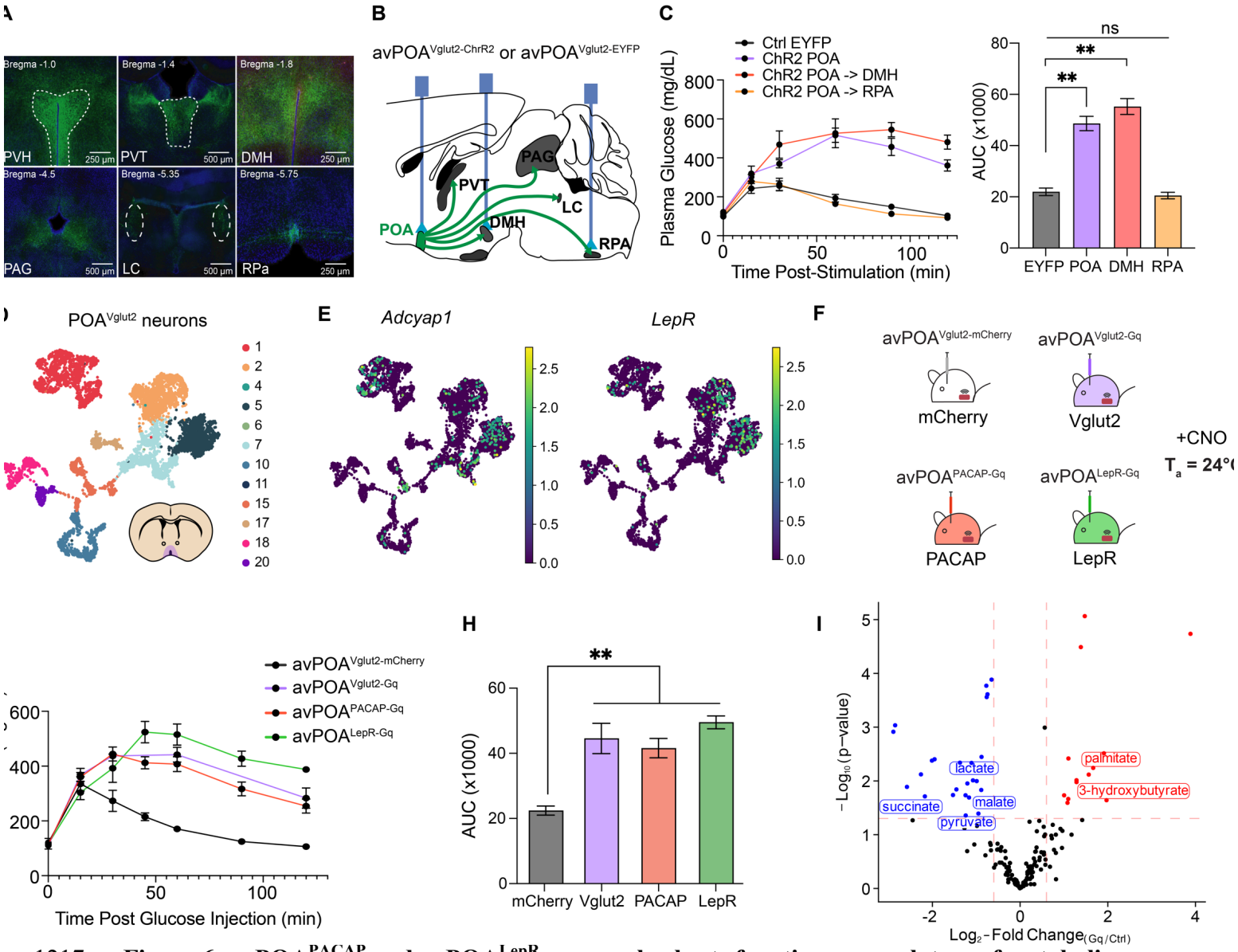

Figure 6: avPOA^{PACAP} and avPOA^{LepR} neuronal subsets function as regulators of metabolic flexibility. (A) Immunostaining of axonal fibers in *Vglut2-IRES-Cre* mice transduced with Gq-DREADD (AAV-hSyn-DIO-hM3D(Gq)-mCherry). Axonal projections were identified in a variety of downstream regions, including the paraventricular thalamus (PVT), paraventricular hypothalamus (PVH), dorsomedial hypothalamus (DMH), periacqueductal grey (PAG), locus coeruleus (LC), and raphe pallidus (RPa). **(B)** Optogenetic branch stimulation of hindbrain-projecting avPOA^{Vglut2} neurons. Blue bars correspond to regions targeted for optogenetic stimulation via cannula implantation and subsequent exposure to 455 nm blue light. **(C)** (*Left)* Glucose tolerance testing of *Vglut2-IRES-Cre* animals transduced with a Cre-dependent ChR2 (AAV-DIO-ChR2(H134R)-EYFP) or EYFP (AAV-DIO-EYFP) with optic fibers placed

1227 unilaterally above either the POA, POA→DMH-projecting neurons, or POA→RPA-projecting
1228 neurons. *(Right)* AUC of GTT for each cohort described (ns = $p > 0.05$, ** = $p < 0.005$, student's
1229 two-tailed t-test, mean ±SEM, n = 4 EYFP, n = 4 POA, n = 3 POA→DMH, n = 3 POA→RPa
1230 *Vglut2-IRES-Cre* animals). **(D)** UMAP plot and Leiden clustering of all $avPOA^{Vglut2}$ neurons
1231 identified in Hrvatin et al., 2020. **(E)** UMAP plot of $avPOA^{Vglut2}$ neurons colored by *Adcyap1*
1232 and *LepR* expression. **(F)** Schematic showing four groups of animals: mCherry (mCherry-
1233 transduced *Vglut2-IRES-Cre,* n = 11), Vglut2 (Gq-DREADD transduced *Vglut2-IRES-Cre*)
1234 (n=10), PACAP (Gq-DREADD-transduced *PACAP-2A-Cre*) (n=11), and LepR (Gq-DREADD-
1235 transduced *LepR-IRES-Cre* (n=3) animals injected with 1 mg/kg CNO. **(G)** Glucose tolerance
1236 test of mCherry ($avPOA^{Vglut2\text{-}mCherry}$), Vglut2 ($avPOA^{Vglut2\text{-}Gq}$), PACAP ($avPOA^{PACAP\text{-}Gq}$), and
1237 LepR ($avPOA^{LepR\text{-}Gq}$), animals from (F). **(H)** AUC analysis for (G) (** = $p < 0.05$, student's two-
1238 tailed t-test, mean ±SEM, n=7 $avPOA^{Vglut2\text{-}mCherry}$, n = 10 $avPOA^{Vglut2\text{-}Gq}$, n = 11 $avPOA^{PACAP\text{-}Gq}$,
1239 n = 3 $avPOA^{LepR\text{-}Gq}$ animals). (**I**) Volcano Plot of 120-minute polar metabolomics of *PACAP-2A-*
1240 *Cre* animals transduced with a Cre-dependent Gq-DREADD and injected with either PBS or
1241 CNO (1 mg/kg). Animals were treated as in **Figures 2a-c**. Selected overrepresented and
1242 underrepresented metabolites labeled in red and blue, respectively. p-values calculated using
1243 two-tailed t-test; red lines corresponding to p-value and Log_2-Fold changes set at $p < 0.05$ and
1244 $|Log_2\text{-Fold change}| > 0.6$.

Supplementary Figures

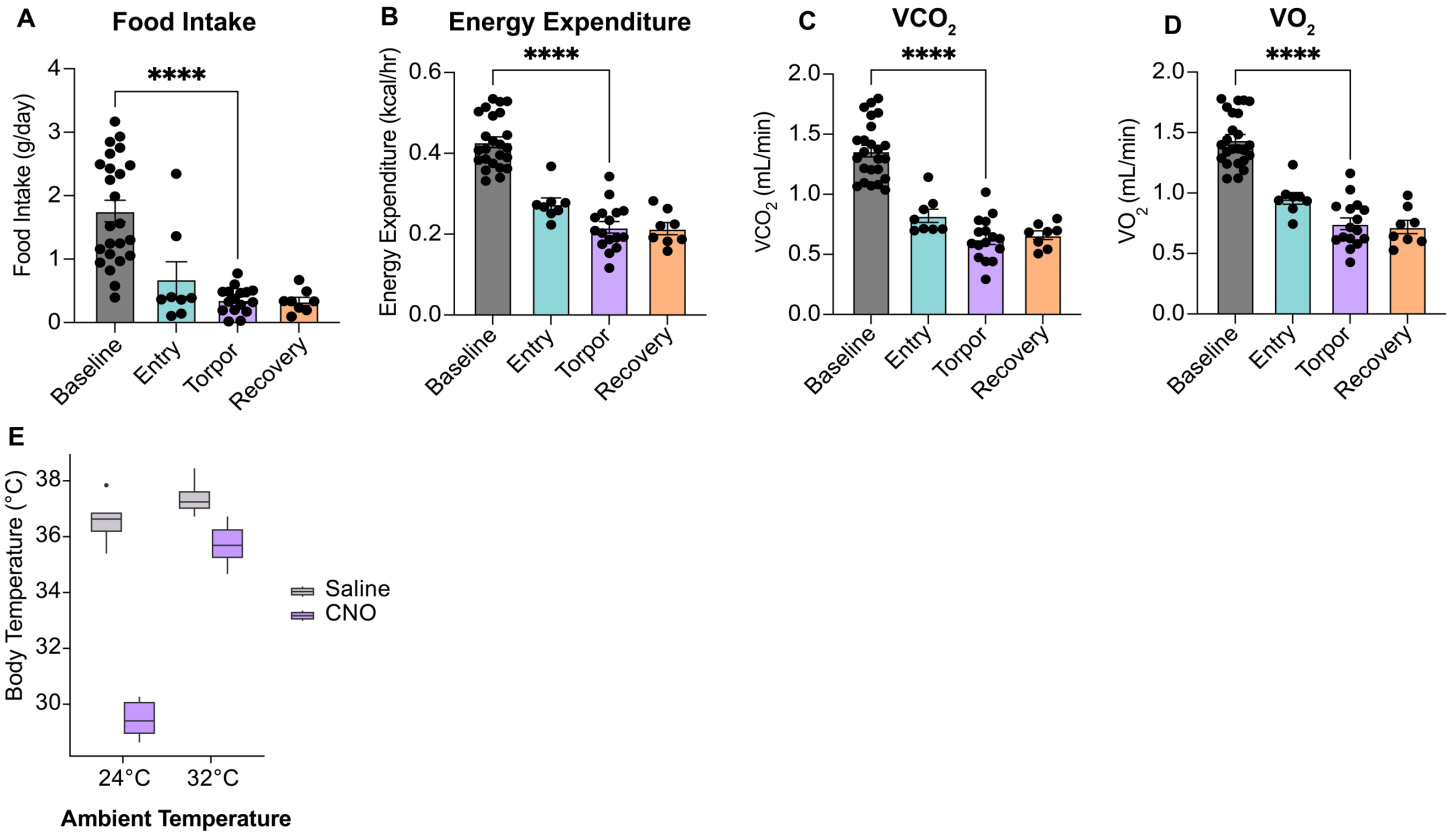

Supplementary Figure 1: avPOA stimulation regulates diverse metabolic parameters. (A-D) Quantitation of (**A**) Food Intake, **(B)** Energy Expenditure, **(C)** VCO_2, and (**D**) VO_2 throughout different phases of avPOA stimulation described in **Figures 1c-f**. Baseline = pre-CNO stimulation, Entry = 60 minutes post-CNO stimulation, Torpor = duration of torpor bout, Recovery = post-torpor period before returning to euthermia (**** = $p < 0.00005$, mean ±SEM, student's two-tailed t-test, n = 8 WT C57Bl/6J mice). **(E)** Quantitation of animal body temperature following 300 minutes of saline or Gq-DREADD stimulation at either T_a =24°C or 32°C (n = 8, mean ±SEM).

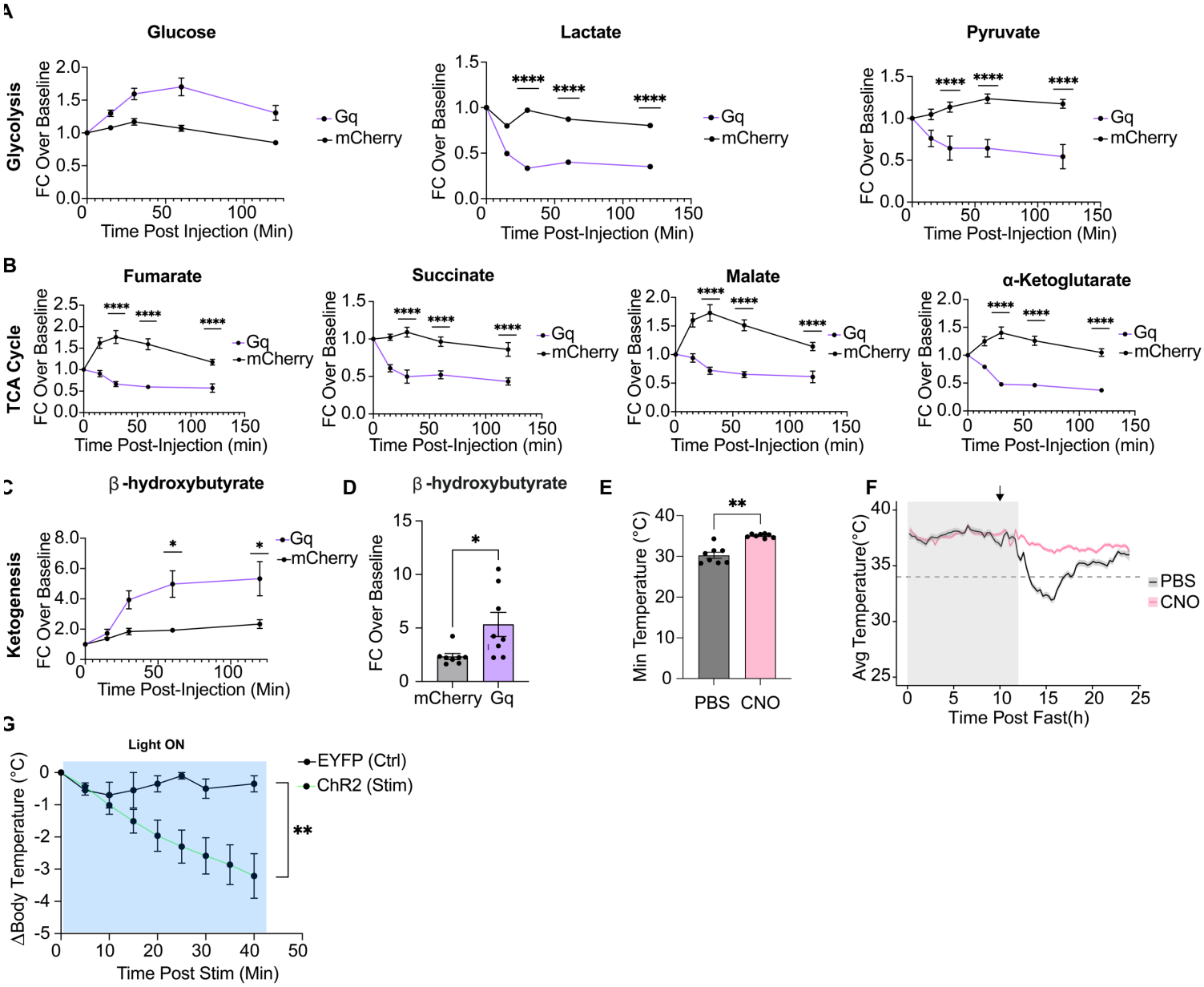

Supplementary Figure 2: TCA cycle and glycolytic metabolite abundance is altered following CNO stimulation. (A) Major glycolytic metabolites, including pyruvate and lactate, are monotonically decreased by CNO stimulation of Cre-dependent mCherry- or Gq-DREADD-transduced *Vglut2-IRES-Cre* mice as compared to their saline-injected counterparts. Conversely, glucose is monotonically increased upon CNO stimulation as compared to saline injection (** = $p < 0.005$, **** = $p < 0.00005$, student's two-tailed t-test, mean ±SEM, n = 8 animals). **(B)** Significantly downregulated TCA cycle metabolites include fumarate, succinate, malate, and α-ketoglutarate (**** = $p < 0.00005$, student's two-tailed t-test, mean ±SEM, n = 8 animals). Sample values reported as cohort-specific baseline-normalized fold change. Blood was collected

1262 at 0, 15, 30, 60, 120 minutes post-injection. **(C)** β-hydroxybuyrate levels are significantly
1263 increased in CNO-injected animals as compared to controls (* = $p < 0.05$, student's two-tailed t-
1264 test, mean ±SEM, n = 8 animals). **(D)** Quantitation of (C) 120 minutes after CNO stimulation in
1265 mCherry and Gq animals (* = $p < 0.05$, student's two-tailed t-test, mean ±SEM, n = 8 animals).
1266 **(E)** Quantification of minimal T_b measured during fasting-induced torpor in Gi-DREADD-
1267 transduced *Vglut2-IRES-Cre* animals. Animals were fasted for 24 hours at the beginning of the
1268 dark cycle (ZT 12), and either PBS or CNO (10 mg/kg) was injected 10 hours after fasting began
1269 (ZT 22) (** = $p < 0.005$, student's two tailed t-test, n = 8 PBS, n = 8 CNO, same animals, mean
1270 ±SEM). **(F)** Longitudinal trace of animals in (E), demonstrating that Gi-DREADD animals
1271 injected with CNO do not go into torpor due to inhibition of $avPOA^{Vglut2}$ neurons, whereas PBS-
1272 injected animals enter normally. Arrow corresponds to time of CNO or PBS injection. Gray
1273 shading indicates dark cycle (ZT12-24). Horizontal dashed line at 34.5°C corresponds to the
1274 temperature threshold for torpor entry. **(G)** Stimulation of $avPOA^{Vglut2}$ neurons with 455 nm light
1275 decreases body temperature in ChR2-, but not EYFP-expressing animals over the 40-minute time
1276 period of blue light stimulation (* = $p < 0.05$, student's two-tailed t-test, mean ±SEM, n = 4
1277 EYFP and n = 5 ChR2 animals).

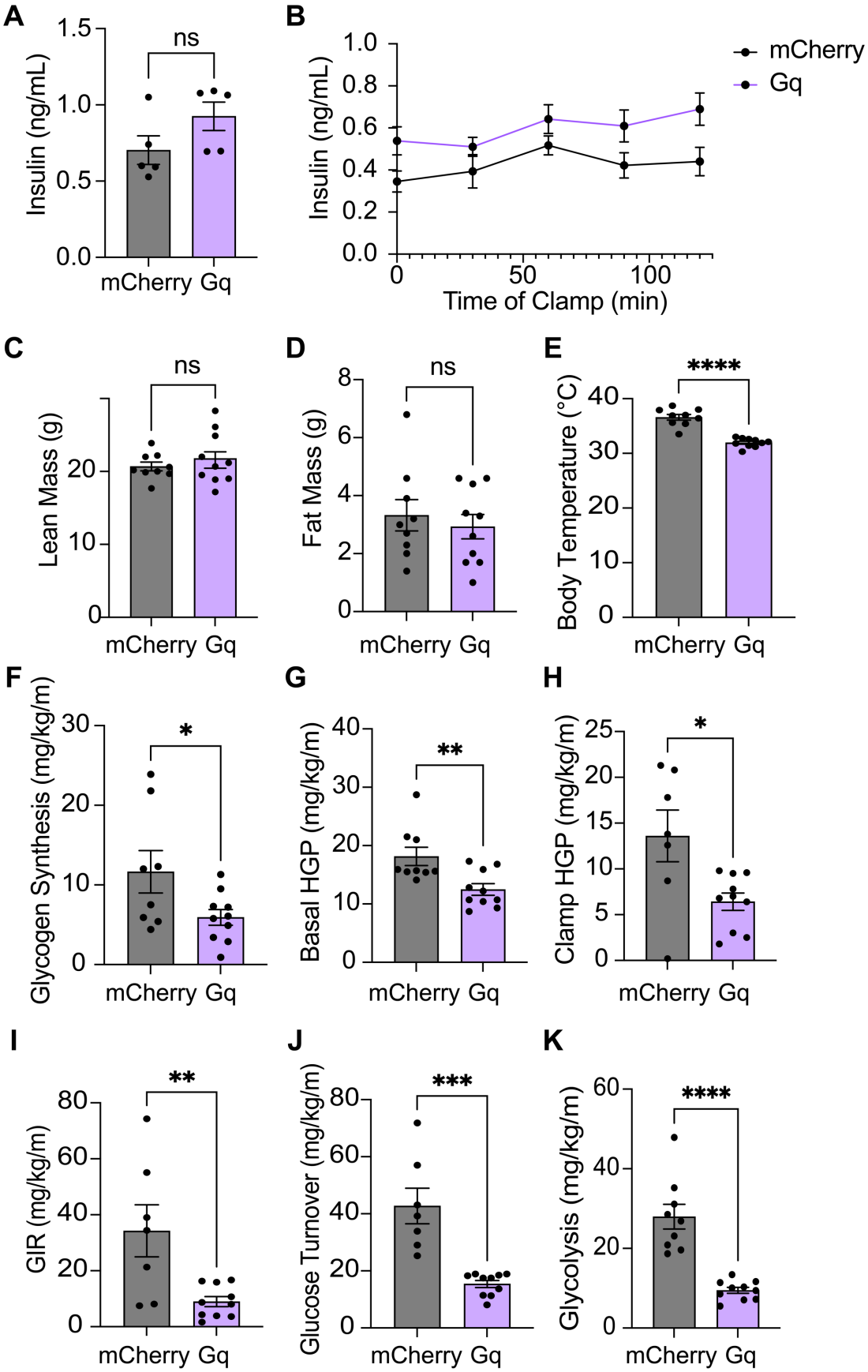
A
Insulin (ng/mL)
1.5
1.0
0.5
0.0
ns
mCherry Gq
B
Insulin (ng/mL)
1.0
0.8
0.6
0.4
0.2
0.0
0
50
100
Time of Clamp (min)
mCherry
Gq
C
Lean Mass (g)
ns
mCherry Gq
D
Fat Mass (g)
ns
mCherry Gq
E
Body Temperature (°C)
****
mCherry Gq
F
Glycogen Synthesis (mg/kg/m)
*
mCherry Gq
G
Basal HGP (mg/kg/m)
**
mCherry Gq
H
Clamp HGP (mg/kg/m)
*
mCherry Gq
I
GIR (mg/kg/m)
**
mCherry Gq
J
Glucose Turnover (mg/kg/m)
***
mCherry Gq
K
Glycolysis (mg/kg/m)
****
mCherry Gq

1278 **Supplementary Figure 3: Hyperinsulinemic-euglycemic clamp physical and clamp**
1279 **parameters. (A)** Quantification of glucose and insulin levels in plasma of fed *Vglut2-IRES-Cre*
1280 animals expressing Cre-dependent mCherry or Gq-DREADD in the avPOA, 60 minutes post-
1281 CNO injection ($p<0.005$ = **). **(B)** Hyperglycemic clamp experiment monitoring plasma insulin
1282 levels for 120 minutes during administration of various concentrations of glucose. Blood samples
1283 were taken at 0, 30-, 60-, 90-, and 120-minute time points throughout the experiment (n = 9
1284 mCherry, n = 10 Gq-DREADD animals). **(C-K)** correspond to the hyperinsulinemic-euglycemic
1285 clamp described in **Figure 3**. (**C)** Lean mass of animals analyzed by Dual X-ray Absorptiometry
1286 (DEXA) prior to beginning of the clamp. (**D)** Fat mass analyzed by DEXA prior to beginning of
1287 the clamp. (**E)** Average temperature of animals throughout the duration of the clamp. **(F)**
1288 Glycogen synthesis calculated during the clamp based on relative incorporation of ^{3}H into
1289 hepatic glycogen pool. (**G)** Hepatic Glucose Production (HGP) prior to initiation of the clamp as
1290 determined by the ratio of basal ^{3}H-Glucose infusion to the specific activity of plasma glucose
1291 prior to the initiation of the clamp. (**H)** Insulin-stimulated Hepatic Glucose Production during the
1292 clamp, determined by the difference between glucose infusion and whole-body glucose turnover
1293 rates. Insulin-stimulated HGP reflects the action of insulin on the liver specifically. **(I)** Glucose
1294 infusion rate (GIR) for each cohort. GIR was taken as an average over the duration of the
1295 experiment. Decreased GIR in Gq-DREADD-expressing animals indicates insulin insensitivity.
1296 Two control animals were excluded from analysis, as GIR measurements were highly irregular.
1297 **(J)** Glucose turnover in each cohort throughout the duration of the clamp, calculated as the ratio
1298 of ^{3}H-glucose infusion to plasma glucose specific activity during the final 30 minutes of the
1299 clamp. (**K)** Whole-body glycolysis estimated based on glycogen synthesis, GIR, and glucose
1300 clearance rates throughout the experiment (n = 9 mCherry, n = 10 Gq-DREADD, * = $p < 0.05$,
1301 ** = $p < 0.005$, *** = $p < 0.0005$, **** = $p < 0.00005$, two-tailed t-test).

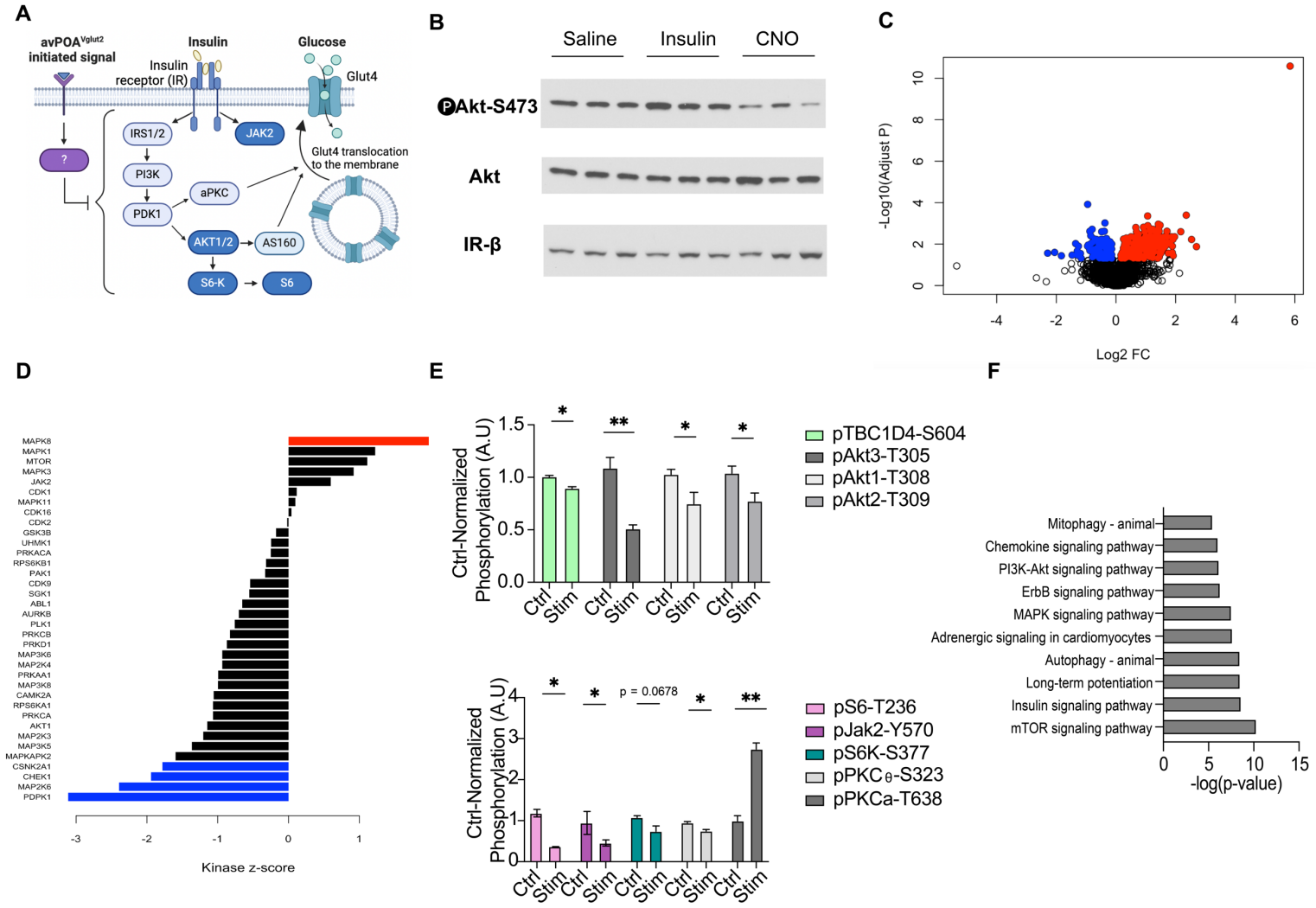

Supplementary Figure 4: Phosphoproteomic analysis of skeletal muscle reveals avPOA-induced defects in insulin signaling. (A) Schematic depicting the insulin signaling pathway and relevant downstream consequences of its activation with respect to glucose uptake. (**B)** Western blot of gastrocnemius muscle lysates obtained from mice injected with either saline, insulin, or CNO showing reduced Akt phosphorylation in CNO-injected animals as compared to saline-injected animals. **(C)** Volcano plot of differentially phosphorylated peptides in the gastrocnemius muscles of *Vglut2-IRES-Cre* mice transduced with Cre-dependent Gq-DREADD in the avPOA and injected with CNO as compared with saline. Significance threshold of $p < 0.05$ and Log_2FC of 0.6 used to determine significantly "hyperphosphorylated" or "hypophosphorylated" peptides. Red points correspond to peptides hyperphosphorylated in CNO relative to saline control, while blue correspond to hypophosphorylated peptides. **(D)** Kinase-substrate enrichment analysis score

1313 of various kinases identified within the dataset in CNO vs. saline control animals. Kinases whose
1314 substrates demonstrated hyperphosphorylation in CNO vs. saline control muscles were scored
1315 higher, and those that were significant are shown in red. Kinases whose substrates demonstrated
1316 hypophosphorylation in CNO vs. saline control were scored lower, and those that were
1317 significant are shown in blue. Z-score cutoff of |1.5| was used to determine significance. **(E)**
1318 Saline-normalized phosphorylation of individual residues in key proteins in the insulin signaling
1319 pathway (n = 3 animals per cohort, * = $p < 0.05$, ** = $p < 0.005$, student's two-tailed t-test). **(F)**
1320 GO-Term analysis of peptides that demonstrated significant ($p < 0.05$) hypophosphorylation in
1321 CNO vs. control animals.

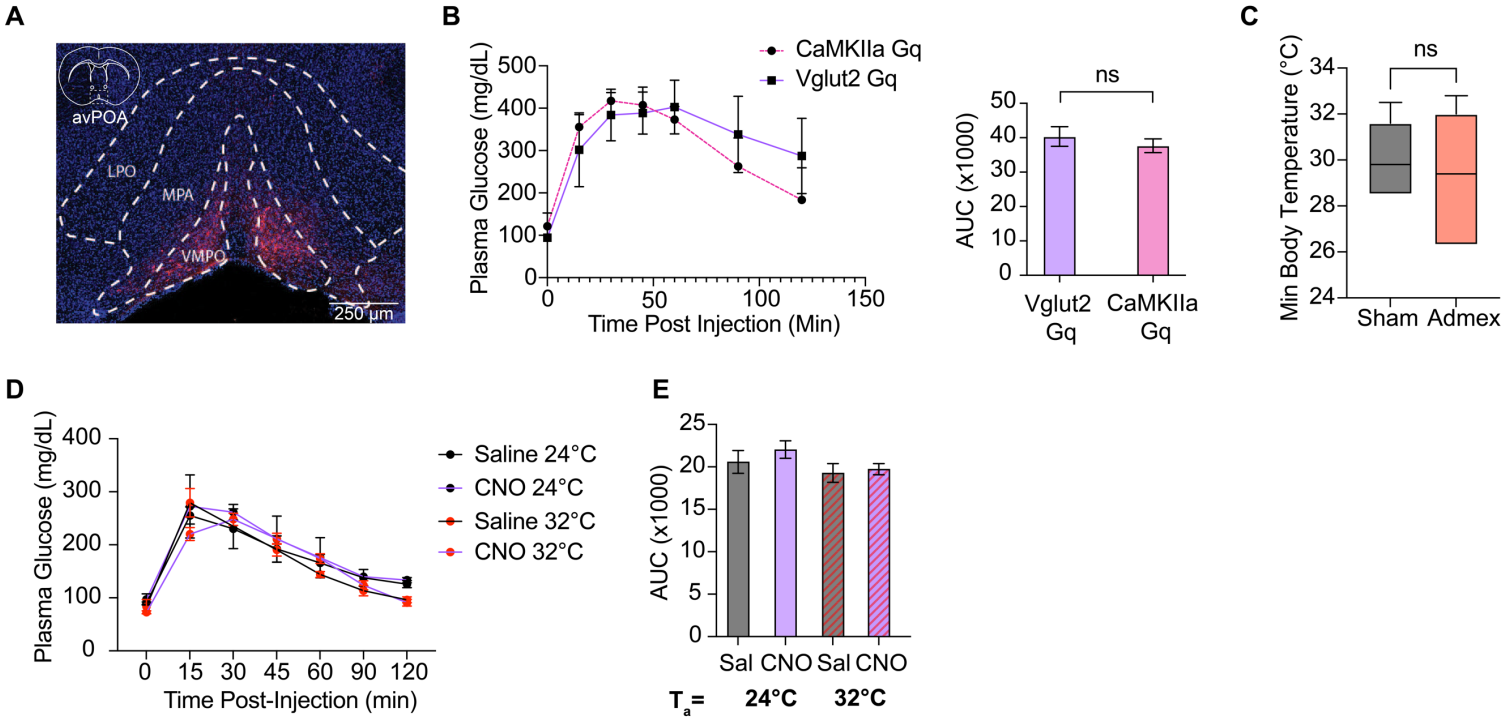

Supplementary Figure 5: Validation of CaMKIIa-Gq efficiency in adrenalectomized animals. (A) Representative image of an Admex mouse transduced with CaMKIIa-Gq-DREADD (AAV-CaMKIIa-hM3D(Gq)-mCherry). **(B)** (*Left*) Comparison of the efficiency of avPOA^{Vglut2} stimulation during a GTT using a CaMKIIa-Gq as compared with a DIO-Gq (AAV-hSyn1-DIO-hM3D(Gq)-mCherry) used in B6 and *Vglut2-IRES-Cre* animals, respectively. (*Right*) No statistically significant difference was observed between the two cohorts (ns = $p > 0.05$, student's two tailed t-test, mean ±SEM, n = 7 CaMKIIa-Gq, 8 Vglut2-Gq animals). **(C)** Minimum body temperatures achieved by both Sham and Admex animals transduced in the avPOA with CaMKIIa-Gq-DREADD and injected with CNO (ns = $p > 0.05$, n= 5 Sham, n=7 Admex animals, student's two-tailed t-test). **(D)** Comparison of CaMKIIa-Gq-DREADD Admex mice in a GTT under the following paradigms: –CNO 24°C, +CNO 24°C, -CNO 32°C, and +CNO 32°C, demonstrating nearly unchanged glucose tolerance between conditions (ns = $p > 0.05$, mean ±SEM, n=8 Admex animals, student's two-tailed t-test). **(E)** AUC quantitation of (D).

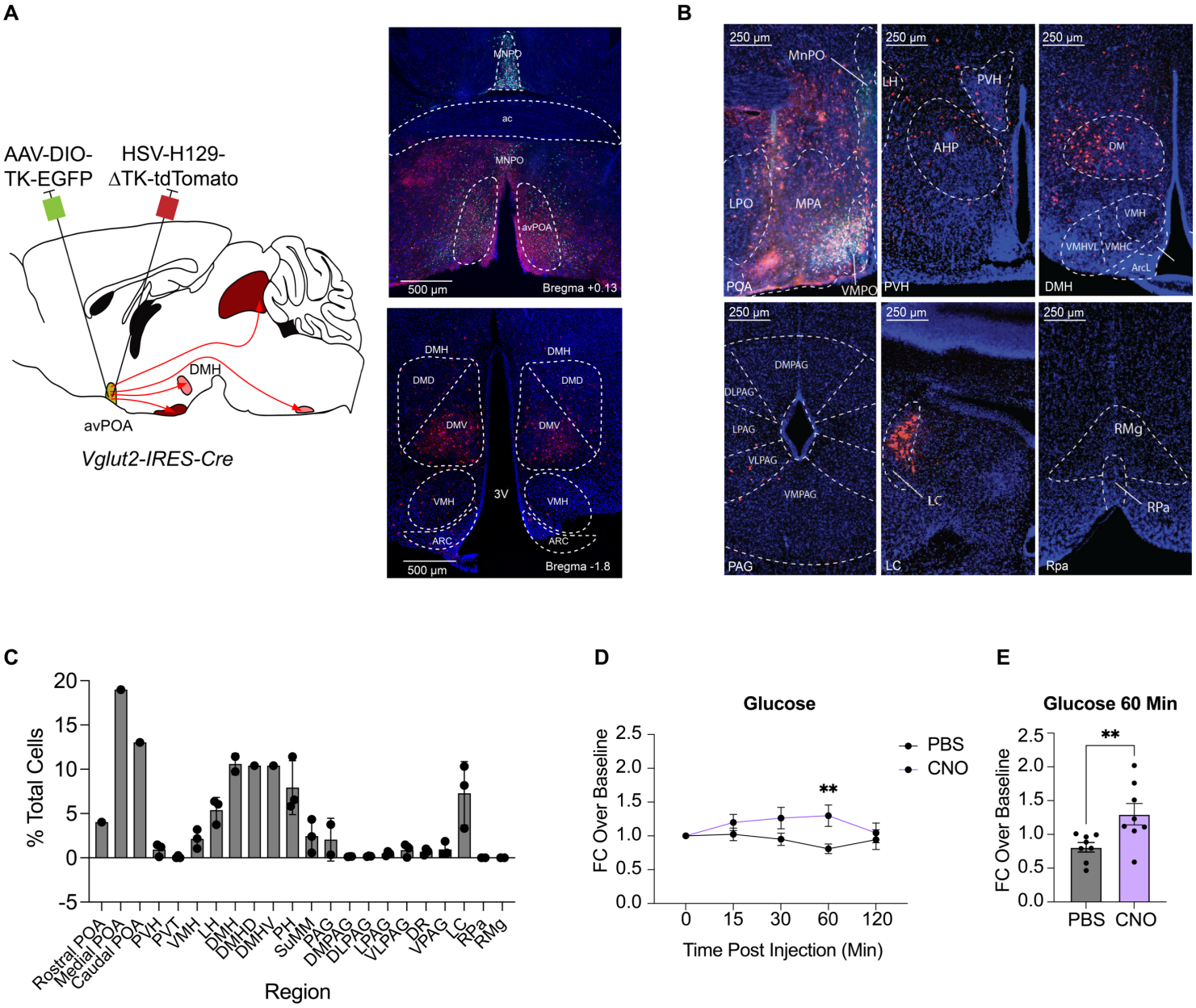

1340 **Supplementary Figure 6: avPOA neurons project to diverse regions, which may have**
1341 **distinct effects on body temperature and blood glucose.** (**A**) (*Left*) Schematic for
1342 administration of AAV helper virus and HSV anterograde tracer to the avPOA of *Vglut2-IRES-*
1343 *Cre* animals. Mice were first transduced with a complementary helper AAV (AAV-DIO-TK-2A-
1344 EGFP), and after a two-week recovery period were transduced in the same region with HSV-
1345 H129-ΔTK-tdTomato, and sacrificed 65 hours following injection (n=3 *Vglut2-IRES-Cre*
1346 animals). (*Right*) (*Top*) Representative image of the starter region of the avPOA and (*Bottom*)

1347 one of the downstream targets of avPOA^{Vglut2} neurons in the dorsomedial hypothalamus (DMH).
1348 HSV^{+} cells labeled in red, AAV-DIO-TK-EGFP^{+} starter cells labeled in green. Note: in the
1349 DMH, HSV^{+} cells predominantly are observed in the ventral portion of the DMH (DMV). (**B)**
1350 Representative images of the same regions as **Figure 6a** in mice transduced with the anterograde
1351 monosynaptic tracer HSV-H129-ΔTK-tdTomato. (**C**) Quantitation of HSV expression in (B).
1352 Regions were defined in accordance with the Paxinos Reference Atlas, and the number of HSV-
1353 positive cells as a fraction of total DAPI cells was calculated for each region (n = 3 *Vglut2-IRES-*
1354 *Cre* animals, mean ±SEM). **(D)** Fold change in plasma glucose concentrations of *PACAP-2A-Cre*
1355 animals described in **Figure 6i** injected with either PBS or CNO at t = 0, 15, 30, 60, and 120
1356 minutes post-injection relative to baseline (** = $p < 0.005$, student's two tailed t-test, n = 8 PBS,
1357 n = 8 CNO, mean ±SEM). **(E)** Quantification of glucose levels of individual animals from (D) at
1358 t = 60 minutes post-injection (** = $p < 0.005$, student's two tailed t-test, n = 8 PBS, n = 8 CNO,
1359 mean ±SEM).

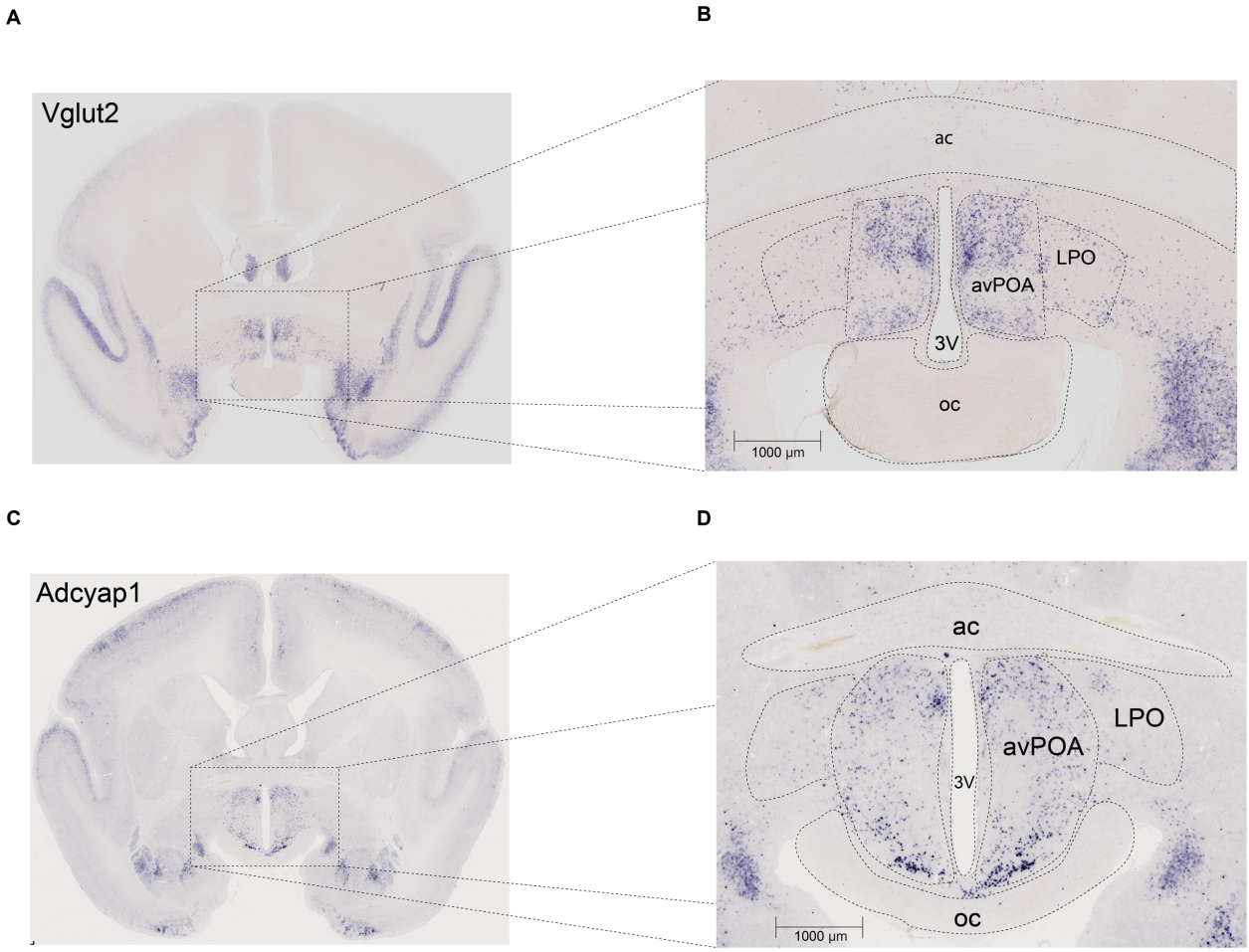

Supplementary Figure 7: avPOA expression of *Vglut2* and *Adcyap1* in the marmoset brain. **(A)** RNA fluorescence *in situ* hybridization (FISH) image of *Vglut2* RNA expression in coronal marmoset brain region corresponding to mouse avPOA. Purple puncta indicate *Vglut2* RNA expression. **(B)** Magnification of (A) to show the avPOA and LPO regions that correspond to the mouse brain, demonstrating that avPOA^{Vglut2} expression is anatomically conserved between species. **(C)** RNA FISH image of *Adcyap1* RNA expression in coronal marmoset brain region corresponding to mouse avPOA. Purple puncta indicate *Adcyap1* RNA expression. **(D)** Magnification of (C) to show the avPOA and LPO regions that correspond to the mouse brain, demonstrating that avPOA^{Adcyap1} expression is anatomically conserved between species. Images adapted from: https://gene-atlas.brainminds.jp/